UNIVERSITÀ DEGLI STUDI DI PADOVA

Dipartimento di Fisica e Astronomia "Galileo Galilei"

Master Degree in Astrophysics and Cosmology

Final Dissertation

The non-LTE copper abundance of the Sun

Thesis supervisor:
Prof. Antonino Milone

Candidate:
Mila Racca

Thesis co-supervisor:
Dr. Karin Lind

Academic Year 2021/22

"I saw the Aleph from every point and angle, and in the Aleph I saw the earth and in the earth the Aleph and in the Aleph the earth; I saw my own face and my own bowels; I saw your face; and I felt dizzy and wept, for my eyes had seen that secret and conjectured object whose name is common to all men but which no man has looked upon: the unimaginable Universe."

The Aleph - J. L. Borges

"Vidi l'Aleph, da tutti i punti, vidi nell'Aleph la terra e nella terra di nuovo l'Aleph e nell'Aleph la terra, vidi il mio volto e le mie viscere, vidi il tuo volto, e provai vertigini e piansi, poiché i miei occhi avevano visto l'oggetto segreto e supposto, il cui nome usurpano gli uomini, ma che nessun uomo ha contemplato: l'inconcepibile Universo."

L'Aleph - J. L. Borges

Contents

Acknowledgements

I want to express my sincere gratitude to my supervisor, Dr. Karin Lind, for the opportunity that she gave me, for her trust, support and precious advices and for the project that she assigned me, which turned out to be as challenging as interesting. A very special thanks goes to Gloria and Cis for their patience and for their continuous help, and to Bart, Anna, Quentin, Ivo and Jack, for being such good colleagues and, above all, friends. All of them, each in their own special way, enriched my Erasmus experience in Stockholm, making me feel at home every single day. I want to thank also Prof. Antonino Milone for giving me the biggest opportunity I could have asked for, for his trust and kindness.

Vorrei ringraziare i miei genitori, Lauretta e Livio, per essersi presi cura di ogni mia ambizione, nonostante queste mi abbiano portata sempre più lontana da loro. Il vostro supporto prezioso mi ha permesso di fare esperienza di un numero di città, atmosfere, culture e persone che mai avrei immaginato di poter conoscere, oltre all'opportunità di studiare la scienza più affascinante di questo mondo.
Ringrazio ancora di cuore Gloria, per il supporto costante e per l'amicizia che ha saputo donarmi sin dal primo momento dentro lo Spaghetti Office. Insieme a lei ringrazio Mirko. Siete stati dei compagni di viaggio meravigliosi e avete reso Stoccolma molto meno fredda del previsto.
Chi mi conosce però sa quanto sia stata Padova a cambiarmi maggiormente. Insieme a Lei, ringrazio chi ha reso le sue strade così speciali. Un ringraziamento particolare va ad Adri perchè ci siamo sempre prese cura l'una dell'altra e siamo arrivate alla fine passo dopo passo, ciambella dopo ciambella, pizza dopo pizza e chiacchierata dopo chiacchierata. Sei stata come una sorella in questi anni. Grazie a Kai e Andrea perchè mi sono divertita da matti con voi. Grazie a Claudia, Maria Paola e Maria Francesca per la vostra sincerità, che mi ha insegnato nuovamente il valore della vera amicizia. Grazie a Fra, Ale e Fede per le belle serate, il supporto e i consigli letterari.
Ringrazio inoltre Aurora ed Elisa, perchè nonostante migliaia di chilometri ci separassero, ci sono sempre state.
Grazie ai miei amici e alle mie amiche di Savigliano, da cui torno sempre con gioia.

Anche se siamo tutti sparsi per il mondo, siete il mio porto sicuro, fonte di risate autentiche. La mia gratitudine va soprattutto a Idarosa perchè non ho mai conosciuto una persona così diversa da me e, allo stesso tempo, così simile. Non so bene come, ma accade che le nostre emozioni danzino all'unisono e che lei mi capisca sempre. Nonostante le nostre divergenze, ha sempre per me la parola giusta al momento giusto e non potrei chiedere di più.
Infine, ringrazio Davide. Lui si muove nel mondo in punta di piedi, con bontà e rispetto, ma anche con dignità e ambizione. Ha una percezione della realtà rara e preziosa e mi ha insegnato a trovare la Meraviglia dove prima i miei sensi erano silenti. Caro Da, non so più come esprimere la mia gratitudine nei tuoi confronti, e tutto quello che penso già lo conosci. Allora, proverò a mettere a parole quello che siamo stati in questi lunghi anni di distanza. Quando tutti gli alberi dell' Europa continentale erano in fiore già da lunghe settimane, a Stoccolma ho visto il primo bocciolo. In Svezia il freddo dura a lungo e la primavera si fa attendere. Ma l'aspetto più snervante di tutti era che sapevo perfettamente che altrove i fiori erano sbocciati da tempo, mentre io ero circondata da alberi spogli. Averti distante, durante questi anni, è stato come aspettare la primavera a Stoccolma. Sapevo che il fiore più bello c'era, ma che era a chilometri di distanza. Allora ho aspettato, ti ho aspettato, mi hai aspettata, e quando ci siamo ritrovati è scoppiata la primavera più bella di tutte.

Abstract

In this work, I explore stellar spectroscopy's state of the art, by inferring the Solar abundance of copper in thermodynamic equilibrium (LTE) and non-local thermodynamic equilibrium (NLTE). I present a new model atom based on the latest released atomic data. The energy levels and bound-bound transition data were taken from the spectroscopic line calculation performed by Kurucz (1999). The hydrogen collisions data recently published by Belyaev et al. (2020). The accurate oscillator strengths for all the line transitions in model atom and photoionization cross sections were calculated by Liu et al. (2014), using the R-matrix method in the Russell–Saunders coupling scheme. The electron collisions rate were computed with a semi-empirical recipe by van Regemorter.
The line formation for neutral copper was performed using the radiative transfer code Balder (Amarsi et al. (2019)) with a one-dimensional solar atmosphere, including 125 terms of Cu I and 25 states of Cu II. I show the chemical analysis computed on five spectral lines of Cu I, by using the synthesis method. The lines were chosen from a set of twelve lines studied by Shi et al. (2014) and for each of them the hyperfine structure was taken into account. Our study confirms that the main NLTE mechanism for Cu II is ultraviolet overionization, which leads to positive abundance corrections if NLTE is assumed. All the lines indeed produce a greater copper abundance if studied in NLTE. The mean value for Cu abundance obtained in NLTE is $log_{\epsilon_\odot} A(Cu) = 4.29 \pm 0.10$, while it is $log_{\epsilon_\odot} A(Cu) = 4.17 \pm 0.11$ in LTE. Both the results are in accordance with different works in literature. However, the difference between the abundance in NLTE and LTE (0.12 dex) is higher than the one found by Shi et al. (2014) ($\sim$ 0.02 dex), and this is probably due to the different data sets used for inelastic collisions with hydrogen. The synthetic lines, generated with the radiative transfer code Balder, do not fit the observed spectral lines perfectly, which is probably due to the 1D approximation. In 1D model, the convective motions on the stellar surfaces are described by setting the microturbulence velocity as a fixed parameter. Non-LTE radiative transfer calculations with three-dimensional hydrodynamic model atmospheres are needed to correct this discrepancy.

Chapter 1

Introduction

Spectroscopy is the key to unlock the information encoded in starlight. Stellar spectra have numerous absorption lines that allow for the extraction of fundamental properties (e.g. surface density and temperature) and can be used to categorize stars according to spectral type. The precise wavelength position of spectral lines is a tracer of stellar dynamics, and it has recently been used to show the presence of a large black hole in the centre of our galaxy, as well as the presence of planets orbiting stars other than the Sun. Moreover, the intensity of stellar absorption lines compared to the continuum may also be used to calculate the **abundances of elements** in the stellar photosphere and therefore explore the chemical evolution of the Galaxy in a straightforward way. The abundances in stars' photospheres, indeed, reflect the abundances in the molecular clouds from which the stars formed, from which we can trace the origin of the elements as well as the chemical evolution of the galaxies. Studying the chemical evolution of our Galaxy means understanding how and where the elements were formed in the Universe. For example, the chemical composition of extremely metal-poor stars provides unique insight into the early history of the Galaxy and the properties of the first stars, the so-called Population III (Nordlander et al. (2016)). Moreover, the chemical abundance patterns in globular clusters (GCs) show additional complexity that cannot be accounted for by standard models for chemical evolution. In particular, the abundances of many of the light elements deviate from those found in field stars (Bastian and Lardo (2018)), with some elements being enhanced (He, N, Na, Al) and others depleted (C, O, Mg). The underlying cause of these abundance anomalies remains poorly understood. For this reason, all the ongoing studies about chemical abundances are extremely relevant nowadays.
In this work, we focused on copper (Cu). The cosmological history of this element is still enigmatic since we do not know where and when it was synthesised for the first time (see chapter 3.1). The abundance of Cu plays an essential role in the investigations of the chemical evolution of various stars, such as giant stars (McWilliam and

Smecker-Hane (2005). Moreover, it has a unique evolutionary trend as the [Fe/H] varies from extremely metal-poor to solar abundance, but the causes are not completely known. Copper is also relevant in the context of Globular Clusters (GCs) (see chapter 3.3). For example, in Omega Centauri the copper abundance as a function of the metallicity follows a peculiar trend if compared to the other GCs (McWilliam and Smecker-Hane (2005)). This behaviour can reveal important information not only about Omega Centaury itself but also about the evolution of the GCs.

Before talking in detail about all the topics I introduced above, which will be deepened later on, we need to define what a chemical abundance is. There are different ways to define the **abundance of an element**. A common definition is given by eq. 1.1, in which A represents the absolute abundance of an element X. It is given by the logarithm of the ratio between the number of nuclei of an element X and the number of nuclei of hydrogen. In this definition, the hydrogen's abundance is conventionally set at 12.
Another definition of abundance is given in eq. 1.2, which describes the relative abundance of element X with respect to the H abundance. The difference between the absolute abundance of the element in the target star and into the Sun gives this relative abundance. Here a result of [X/H] = 1 would indicate X is 10 times more abundant in the concerned star than in our Sun.

$$A(X) = \log_{10} \frac{N_X}{N_H} + 12 \tag{1.1}$$

$$[X/H] = A_\star(X) - A_\odot(X) \tag{1.2}$$

As already stated, one of the primary goals of stellar spectroscopy is the determination of stellar chemical composition. The intensity of photospheric absorption lines can reveal information about the relative abundances of components in the star's photosphere. In general, this is accomplished by determining the equivalent width of spectral lines (see chapter 2.4.1) or by using the synthesis method (see chapter 2.4.2). The ability to accurately model the line formation process over orders of magnitude in [Fe/H] is crucial for correctly delineating abundance trends as a function of metallicity. Most of the chemical abundance studies in the literature assume **Local Thermodynamic Equilibrium (LTE)** (see Sec. 2.6.1). The essential premise of LTE is that collisions control the energy partitioning of the matter in the medium more strictly than it is controlled by radiation. Thus, the LTE approximation determines the behaviour of the atomic level population and can be used when collisional processes dominate over radiative processes in the atmosphere. Then the source function (ratio of the emission coefficient to the absorption coefficient), can be described by the Planck function and the velocities of particles follow the Maxwell distribution. Additionally, excitation and ionization states

follow the Saha-Boltzmann distribution, defined by the local temperature and gas pressure. In other words, the validity of using the LTE approximation is determined by whether collisional or radiative processes are dominant in the atmosphere of the star we are observing. For late-type stars, for example, LTE is a good assumption in general. However, most of the atoms are affected by **Non Local Thermodyinamc Equilibrium (NLTE)** mechanism, and even though for late-type stars the difference in abundance between LTE and NLTE is small, such effects need to be taken into account (Fuhrmann (2008)). Moreover, what happens if, for example, we are dealing with the atmospheres of early-type stars, which are dominated by radiation processes? In this case, NLTE (see Sec. 2.6.2) handling of line formation and model atmospheres is needed. In non-LTE, the scattering of photons from the surrounding medium accounts for a portion of the local energy emission. Therefore, the radiation field, which is non-local at some frequencies, also influences the source function. In order to determine the distribution of particles among excitation levels and ionization stages, a coupled system of statistical equilibrium and radiative transfer equations must be solved simultaneously. Astronomers say that NLTE processes represent departure mechanisms from LTE since the population of the levels is different and not governed by Boltzmann-Saha equations. If we do not take into account the NLTE mechanisms that affect the atoms, we will obtain not reliable abundance values, since they produce a different line opacity and source function. For example, one of the most important NLTE processes is called over-ionization. In presence of over-ionization, photoionization is so fast that recombination cannot keep up. Thus, it results in a depopulation process for low-lying levels in the atmospheric layers optically thin for ionizing radiation. Neglecting the NLTE mechanism effect, in this case, has the consequence of underestimating the abundance value.

The goal of my research was to create an atomic model of copper in order to quantify its abundance in the Sun, by using the synthesis method both in LTE and NLTE, to highlight the difference in the abundance value we got. The Sun is the star we better know and that we can resolve. For this reason, it is the first star on which astronomers test their atomic models, before using them to infer chemical abundances in other stars. In chapter 2, I report a summary of central topics in the stellar spectroscopy field: radiative transfer, spectral line formation, line broadening mechanisms, local thermodynamic equilibrium (LTE), and non-local thermodynamic equilibrium (NLTE). In chapter 3, I give an overview of copper, treating the most important open questions about this element. According to different studies, indeed, we still do not know exactly when and where copper was synthesised for the first time. Moreover, the biggest part of the works on copper was done in LTE and for this reason, they are affected by uncertainties. In chapter 4, I explain how we built the atomic model taking into account all the necessary radiative and collisional data. I also introduce the radiative transfer code that we used to build the

synthetic spectrum from the atomic model. In chapter 5 are shown the results for five different spectral lines. A study of minimization of the χ^2 was used to infer the best abundance of copper with different resolutions velocities. The conclusions are finally reported in chapter 6.

Chapter 2

Theory of spectroscopy

Accurate abundance calculation requires realistic methods to compute radiative transfer, whose theory is presented in this section. The reference I used to write this chapter are the notes from the course on Astronomical Spectroscopy given by Prof. Ciroi and the lecture notes Radiative Transfer In Stellar Atmospheres by R.J.Rutten (2003).

2.1 Radiative transfer

Let us consider the case of a radiation beam crossing a gas cloud, our goal is to describe what happens during the interaction between the gas cloud and the radiation field. To do so, we consider a surface and an infinitesimal area element dA of the cloud (Fig.2.1). We define the **specific intensity** as the energy flowing through the area dAcosθ per infinitesimal time and frequency interval in a beam propagating in the solid angle dΩ:

$$I_\nu = \frac{dE_\nu}{dA\cos\theta d\nu d\Omega dt} \qquad [\mathrm{erg\,cm^{-2}\,s^{-1}\,Hz^{-1}\,sr^{-1}}]. \tag{2.1}$$

The radiation while propagating interacts with the atoms in the cloud that may absorb or emit energy. The amount of energy added to the beam is described by the **emission coefficient**:

$$\epsilon_\nu = \frac{dE_\nu}{dsdA\cos\theta d\nu d\Omega dt} \qquad [\mathrm{erg\,cm^{-3}\,s^{-1}\,Hz^{-1}\,sr^{-1}}], \tag{2.2}$$

while the amount of energy lost by the beam is given by the **absorption coefficient** k_ν and is equal to:

$$k_\nu I_\nu = -\frac{dE_\nu}{dsdA\cos\theta d\nu d\Omega dt} \quad [\mathrm{erg\,cm^{-3}\,s^{-1}\,Hz^{-1}\,sr^{-1}}]. \tag{2.3}$$

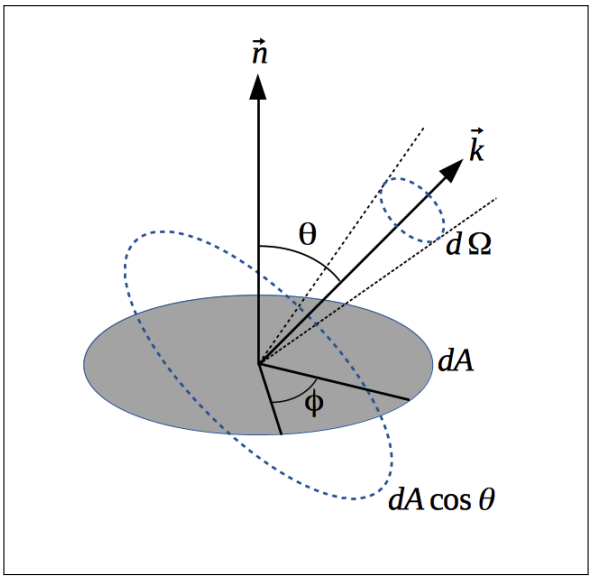

Figure 2.1: A flux of radiation goes through a small portion of a surface. $\vec{n}$ is the normal to the surface, $\vec{k}$ is the direction of propagation. Credits: Notes of the Astronomical Spectroscopy course, given by Prof. Ciroi University of Padova)

The absorption coefficient represents the fraction of energy absorbed from a beam of specific intensity I_ν and it is measured in units of cm^{-1}.
If we consider a radiation beam that propagates into a medium for a geometric path length ds (Fig.2.2), its specific intensity will be affected by energy emission and absorption in the following way:

$$dI_\nu = -k_\nu I_\nu ds + \epsilon_\nu ds, \tag{2.4}$$

from which we obtain the differential form of the **Radiative Transport Equation**:

$$\frac{dI_\nu}{ds} = -k_\nu I_\nu + \epsilon_\nu. \tag{2.5}$$

Assuming the cloud to be along the line of sight to a radiation source, we can create a reference frame with two symmetrical axes: one originating on the side of the cloud facing the source and increasing toward the observer (coordinate **s**), and the other originating on the side of the cloud facing the source and decreasing toward the observer (coordinate **r**). The size of the cloud will be s* in the first case and r* in the second (Fig. 2.3). We can now introduce the concept of **optical depth** τ_ν, which is derived from the following differential equation

$$d\tau_\nu \equiv k_\nu dr = -k_\nu ds, \tag{2.6}$$

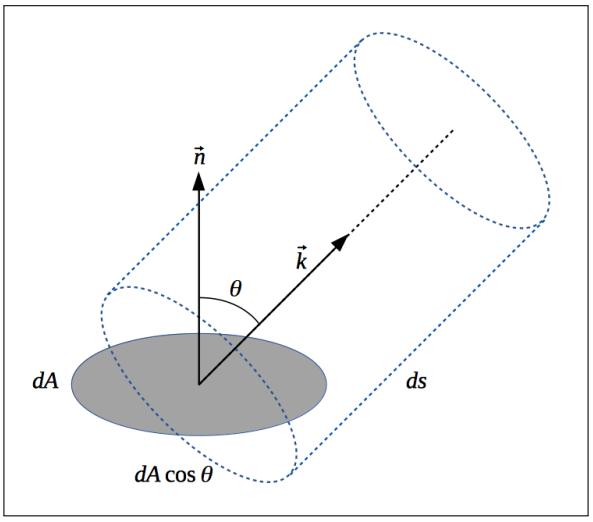

Figure 2.2: A beam of energy flows within a cylindrical volume, where emission and absorption processes take place. Credits: Notes of the Astronomical Spectroscopy course, given by Prof. Ciroi University of Padova)

and will be defined as:

$$\tau_\nu * \equiv \int_0^{r*} k_\nu(r)dr = -\int_{s*}^{0} k_\nu(s)ds. \tag{2.7}$$

Dividing eq. 2.5 by $-k_\nu$, we obtain:

$$\frac{dI_\nu}{d\tau_\nu} = I_\nu - \frac{\epsilon_\nu}{k_\nu} = I_\nu - S_\nu, \tag{2.8}$$

where S_ν is the **source function** and it is independent of the properties of the radiation source and characteristic of the cloud. By integrating equation 2.8 we obtain:

$$\begin{aligned}
&\frac{dI_\nu}{d\tau_\nu} - I_\nu = -\frac{\epsilon_\nu}{k_\nu} \\
&e^{-\tau_\nu}\left[\frac{dI_\nu}{d\tau_\nu} - I_\nu\right] = -\frac{\epsilon_\nu}{k_\nu}e^{-\tau_\nu} \\
&\frac{d}{d\tau_\nu}(I_\nu e^{-\tau_\nu}) = iS_\nu e^{-\tau_\nu} \\
&I_\nu(\tau_\nu = 0) = \int_0^{\tau_\nu^*} S_\nu(\tau_\nu)e^{-\tau_\nu}d\tau_\nu + I_{\nu_0}e^{-\tau_\nu^*},
\end{aligned} \tag{2.9}$$

where $I_{\nu_0} = I_\nu(\tau_\nu^*)$ denotes the intensity of the initial radiation beam as it strikes the cloud on the source's side. The emergent intensity is the sum of the original

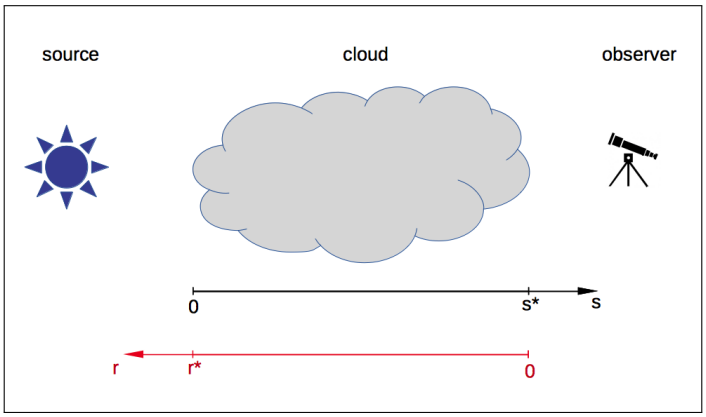

Figure 2.3: The gaseous cloud between the source and the observer. Its dimension is given with respect to two reference systems. They are applied to describe the emission/absorption processes within the cloud. Credits: Notes of the Astronomical Spectroscopy course, given by Prof. Ciroi University of Padova)

specific intensity emitted by the source and attenuated by the entire path across the cloud, and of any contribution originating within the cloud and attenuated by a path corresponding to its own depth. Remembering the expression of the source function, the integral on the right-hand side is equal to:

$$\int_0^{\tau_\nu^*} S_\nu(\tau_\nu) e^{-\tau_\nu} d\tau_\nu = \int_0^{r^*} \epsilon_\nu(\tau_\nu) e^{-\tau_\nu} dr, \tag{2.10}$$

which tells that the total amount of radiation emitted is the sum of contributions attenuated by the appropriate factor $e^{-\tau_\nu}$. In order to solve the integral, we must first understand how S depends on τ_ν. If we assume that S_ν is constant inside the cloud, then:

$$I_\nu(0) = S_\nu(1 - e^{-\tau_\nu^*}) + I_{\nu_0} e^{-\tau_\nu^*} \tag{2.11}$$

This solution has two limits:

- $\tau_\nu \gg 1$ **optically thick case**: $I_\nu(0) = S_\nu$, we can only see the cloud through the source function.
- $\tau_\nu \ll 1$ **optically thin case**: $e^{-\tau_\nu} \approx 1 - \tau_\nu I_\nu(0) \rightarrow I_\nu(0) = \tau_\nu^*(S_\nu - I_{\nu_0}) + I_{\nu_0}$. The emerging intensity is essentially equal to the incoming intensity $I_\nu(0)$ but modified with a very small correction that depends on the source function.

2.1.1 The case of the stellar atmosphere

Consider now the radiation field of a stationary stellar atmosphere as seen by an outside observer. A star does not have the same kind of clearly defined surface as a

rocky planet because it is a fuzzy ball of hot gas. Instead, a star's density decreases more or less smoothly as it moves away from its centre. Fortunately, stars have a sharp transition region called the photosphere that can act as the defining radius. This is the region where, when viewed from the outside, the star abruptly becomes optically thick. The photosphere is the area where a star emits continuum, a type of radiation that has the approximate shape of a black body which results from bound-free and free-free processes in the hot gas. This means that while photons from the photosphere generally reach the observer unhindered, photons that happen to reside at wavelengths where significant bound-bound transitions prevail typically only travel a short distance before being absorbed by the stellar atmosphere. The stellar atmosphere, thus, represents a cold cloud in front of a bright source. The mean free path of the photon, or variable l, is determined by the density and strength of the transition in the absorbing species (a particular atom, ion, or molecule). The mean free path of a photon gets shorter the more likely it is that it will be absorbed by a single species and the more abundant that species is.

The specific intensity I_ν, in this case, is determined by two angles, θ and ϕ, with $\mathrm{d}\Omega = \sin\theta\ \mathrm{d}\theta\mathrm{d}\phi$ (Fig. 2.1). The energy passing through the surface dA per unit time and unit frequency, f_ν, is known as **radiation flux**, and is given by specific intensity integrated across the entire solid angle:

$$F_\nu = \int_\Omega I_\nu cos\theta\ d\Omega = \int_0^{2\pi}\int_0^{\pi} I_\nu cos\theta sin\theta\ d\theta d\phi \tag{2.12}$$

When the radiation field is isotropic, $F_\nu = 0$, but when we observe a flow of radiation toward us, like in a stellar atmosphere, $F_\nu \neq 0$. Indeed, if we assume no azimuthal dependence in I_ν and split it up into outgoing and incoming light, we obtain:

$$F_\nu = 2\pi \int_0^{\pi/2} I_\nu^{out} cos\theta sin\theta\ d\theta + 2\pi \int_{\pi/2}^{\pi} I_\nu^{in} cos\theta sin\theta\ d\theta \tag{2.13}$$

Now, at the stellar surface, we have:

$$\begin{aligned} I_\nu^{in}(0) &= 0 \\ I_\nu^{out}(0) &= \int_0^\infty S_\nu e^{-t_\nu \sec\theta} \sec\theta\ dt_\nu \end{aligned} \tag{2.14}$$

where we assume that the radiation from other stars and galaxies is negligible compared to the star's own radiation. Thus, eq. 2.13 becomes:

$$F_\nu = 2\pi \int_0^{\pi/2}\int_{\tau_\nu}^{\infty} S_\nu e^{-(t_\nu-\tau_\nu)\sec\theta} \sin\theta\ dt_\nu d\theta - 2\pi \int_{\pi/2}^{\pi}\int_0^{\tau_\nu} S_\nu e^{-(t_\nu-\tau_\nu)\sec\theta} \sin\theta\ dt_\nu d\theta \neq 0. \tag{2.15}$$

Let us assume that the stellar atmosphere has a **plane parallel geometry**, and

let us consider a radiation beam passing through a cylindrical volume $dAds$, as shown in Fig. 2.2. We make this assumption because in general, the assumption of a homogeneous medium is not realistic, especially when large scales are considered. So we assume a medium that is optically thick at all frequencies and varies along one axis. In this situation, the atmosphere can be described as a succession of planes with homogeneous properties within each plane. In this case:

$$d\tau_\nu = k_\nu dr \qquad ds = -\frac{dr}{cos\theta}, \tag{2.16}$$

therefore, the radiative transfer equation becomes:

$$\begin{aligned} \frac{dI_\nu(\tau_\nu,\theta)}{ds} &= -k_\nu I_\nu(\tau_\nu,\theta) + \epsilon_\nu \\ cos\theta \frac{dI_\nu(\tau_\nu,\theta)}{d\tau_\nu} &= I_\nu(\tau_\nu,\theta) - S_\nu. \end{aligned} \tag{2.17}$$

The solution is given by the **limb darkening equation**:

$$I_\nu(0,\theta) = \int_0^\infty S_\nu(\tau_\nu) e^{-\tau_\nu sec\theta} d(\tau_\nu \sec\theta), \tag{2.18}$$

where $I_\nu(0,0)$ is the specific intensity at the centre of the stellar disk. If we assume $S_\nu(\tau_\nu) = a_\nu + b_\nu\tau_\nu$, with a_ν and b_ν unknown, we obtain:

$$\begin{aligned} I_\nu(0,\theta) = a_\nu \int_0^\infty e^{-\tau_\nu \sec\theta} d(\tau_\nu \sec\theta) + b_\nu \int_0^\infty \tau_\nu e^{-\tau_\nu \sec\theta} d(\tau_\nu \sec\theta) \\ I_\nu(0,\theta) = a_\nu + b_\nu \cos\theta. \end{aligned} \tag{2.19}$$

Thus, $I_\nu = a_\nu + b_\nu$ at the centre of the disk, while $I_\nu(0,\pi/2) = a_\nu$ at the limb. After measuring the intensity at various angular distances from the centre, a_ν and b_ν can be recovered, as well as the source function's dependence on the optical depth.
The observed flux of radiation at the stellar surface ($\tau_\nu = 0$) is:

$$\begin{aligned} F_\nu(0) &= \int_0^{2\pi} \int_0^{\pi/2} I_\nu(0,\theta) \cos\theta \sin\theta d\theta d\phi \\ F_\nu(0) &= 2\pi \int_0^1 I_\nu(0,\theta) \cos\theta d(\cos\theta), \end{aligned} \tag{2.20}$$

and in the case of the linear source function:

$$\pi F_\nu(0) = 2\pi \int_0^1 (a_\nu + b_\nu \cos\theta) \cos\theta d(\cos\theta) = \pi \left(a_\nu + \frac{2}{3} b_\nu\right), \tag{2.21}$$

from which we obtain the **Eddington-Barbier relation**:

$$F_\nu(0) = S_\nu\left(\tau_\nu = \frac{2}{3}\right) \tag{2.22}$$

It means that the flux emitted at the stellar surface is equal to the source function at optical depth $\tau_\nu = 2/3$.

2.2 Matter-radiation interaction

Most stars have gas surrounding them that is less dense than the star's core. Electrons in the gas's diffuse outer layer can absorb photons of a certain frequency, changing their energy state. Eventually, the electron is de-excited and moves to a lower energy level, emitting a new photon with a certain frequency. Yet, because the re-direction emission is random, there is very little likelihood that it will follow the route of the initial incident photon. Overall, this will result in less intensity of light in an observer's direction at that photon's wavelength. As a result, the spectrum that is produced will exhibit **absorption lines**. These features are produced by the bound-bound transitions. In order to replicate these features of stellar atmospheres, we need to be able to reproduce each photon interaction between emission and absorption. In order to do this, however, it's necessary to introduce some concepts.
Let's consider the general solution of the transport equation again. In order to determine the specific intensity I_ν, we need to know the source function in each point. Thus, it is very important to take into account that, in general, absorption and emission of radiation are due to:

- **continuous processes**, which arises from free-free, free-bound, and bound-free transitions.
- **discrete processes**, generated only by bound-bound transitions.

Therefore, we can separate the two contributions and write the source function as:

$$S_\nu = \frac{\epsilon_\nu^K + \epsilon_\nu^L}{k_\nu^K + k_\nu^L}, \tag{2.23}$$

where K and L are superscripts for continuum and spectral line. In this context is very important to introduce the **Einstein coefficients**:

- the **Einstein spontaneous transition probability coefficient** A_{nm} is equal to the number of transitions $n \to m$ which can occur per unit time (or, equivalently, to the inverse mean lifetime of the level n), from a state n to another state m. The energy of the level n, E_n, is higher than that of level m;
- the **Einstein stimulated emission coefficient** B_{nm} describes the process by which an electron is induced to jump from a higher energy level to a lower one by the presence of electromagnetic radiation at (or near) the frequency of the transition;
- the **Einstein absorption probability coefficient** B_{mn} is used when a photon is absorbed by the atom, causing an electron to jump from a lower energy level to a higher one.

Moreover, in the astrophysical plasma, it is likely to detect emission lines corresponding to forbidden transitions. They occur due to the collisions of free electrons with ions. If v is the relative velocity of an electron with respect to an ion (or a neutral atom), $\sigma(v)$ is the collisional cross-section, and N_e is the electron density, the **collisional rate C** is given by:

$$C = N_e v \sigma(v) = N_e Q(v), \tag{2.24}$$

where Q(v) is the **collisional rate coefficient** and it is expressed in terms of $\mathrm{cm}^3\mathrm{s}^{-1}$.

After exploring these essential concepts, we can now describe the transitions that take place in an atom.

2.3 Spectral lines in stellar spectra

As mentioned above, radiation can be both emitted and absorbed in a number of processes, but we're particularly interested in **bound-bound transitions**. They occur when an electron moves from one bound state to another. Bound states are quantized and their energy spectrum is discrete. For this reason, bound-bound transitions occur only if the energy of the absorbed/emitted photon is exactly equal to the difference between the energies of the two involved states. As a bound-bound transition occurs only across a restricted range of energies and occurs between two clearly defined states of energy, it is only meaningful in a small range of the spectrum. As a result, **bound-bound transitions produce lines**, which have a limited energy range but may undergo significant variations in the particular intensity.
There are five processes that produce an electron transition between two bound levels: radiative excitation, spontaneous de-excitation, induced radiative de-excitation, collisional excitation, and collisional de-excitation.

Radiative excitation

A photon with an energy $h_\nu = E_u - E_l$ can be absorbed by the atom, exciting the electron from the lower level E_l to the upper one E_u. The probability for this process to happen is given by the number of radiative de-excitations per second per particle in state l, which is proportional to the Einstein coefficient that represents this process. The energy states are not infinitely sharp due to Heisenberg's Uncertainty Principle, and therefore one needs to account for the spread in photon energy.

Spontaneous de-excitation

An excited electron can spontaneously decay to a lower level l while emitting a photon with energy $h_\nu = E_u - E_l$. The probability for this process to occur is given

by the Einstein coefficient A_{ul} (given per second per particle in state u). Again, the energy of the emitted photon exhibits a certain spread around the value $E_u - E_l$.

Radiative de-excitation

This process occurs when an electron in the energy state at E_l collides with a free photon with energy $h_\nu = E_u - E_l$, so it jumps to the energy level at E_u. Then a second photon is emitted in the same direction as the first, with an energy equal to h_ν.

Collisional excitation and de-excitation

The transition probability for collisional processes can be defined with the coefficient C_{ul}. This coefficient depends on the type of colliding particles and their speed. Light particles move faster than heavy particles and collide more frequently. For gases where the electron density is similar to the ion density, electron collisions usually dominate. For gases that are nearly neutral, collisions with hydrogen are typically dominant.

2.4 From absorption lines to chemical abundances

The shape of an absorption line depends on the number of photons that are absorbed in a particular wavelength, which depends on the number of atoms of a particular chemical species. Astronomers are able to infer chemical abundances by studying the shapes of the absorption lines. In order to measure the strength of an absorption line from a source we can use two different methods. The first is based on the measurement of equivalent widths (EWs), and the second is on the computation of the synthetic spectrum of the chemical element in question. The two following sections will give a brief description of the two methods.

2.4.1 Equivalent width

The **equivalent width** (EW), which is represented in Figure 2.4, measures the integrated dip of an absorption line and its value is equal to the width of a rectangular piece of spectrum that completely blocks the emergent intensity (flux). It is defined, for the intensity, as:

$$W_\lambda = \int_{\lambda_1}^{\lambda_2} \frac{I_c - I_\lambda}{Ic}\, d\lambda, \tag{2.25}$$

while for the flux, as:

$$W_\lambda^f = \int_{\lambda_1}^{\lambda_2} \frac{F_c - F_\lambda}{Fc}\, d\lambda. \tag{2.26}$$

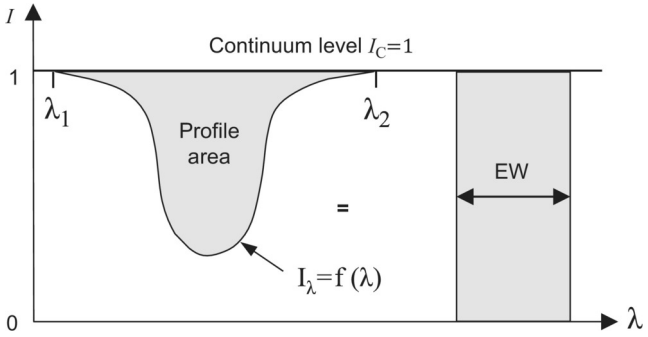

Figure 2.4: The area inside the absorption line is equal to the area of the rectangle. The height of the rectangle is the continuum at the base of the spectral line, and the width is the EW (Credits: Spectroscopy for Amateur Astronomers Trypsteen and Walker (2017))

The rectangular area is supposed to be a direct measure of the number of absorbing atoms that cause an absorption line.

EW is used to quantify the intensity of a spectral line with respect to the continuum. It has the important property of being independent of the flux calibration of the spectrum.

EWs are obtained by either fitting a Gaussian profile for weak lines and a Voigt profile for stronger lines, or simply integrating over the line profile. When lines have a boxy profile due to hyperfine structure components (See sec. 4.1.2), the latter becomes more accurate.

The curve of growth

The **curve of growth (CoG)** is a graph showing how the equivalent width of an absorption line, or the radiance of an emission line, increases with the number of atoms producing the line and with the oscillator strength. However, the relation is not linear at all densities.

The EW is thus a measure of the strength of the line, which can be directly related to the chemical abundance of the element in a star given the stellar parameters, based on the CoG. The CoG is constructed from equivalent widths measured in synthetic spectra. The abundance for a line is found by interpolating the CoG to the observed EW. For weak lines, there is a linear increase of abundance with EWs. Stronger lines lie on the flat part of the curve of growth: they are saturated and thus there is only a weak dependence of the abundance with the EW, which makes them unsuitable as abundance diagnostics. Even stronger lines develop broad wings and form the damping part of the CoG, where the equivalent width has a square root dependence on abundance.

2.4.2 Synthesis

In this method, the elemental abundance is varied until the best fit of a synthetic line profile to the observation is found. The abundance value which better fits the line profile is obtained thanks to a χ-square minimization procedure. This is exactly the method I used in my research and the full description is reported in Chapter 5. Syntheses for each line and star can be computed on the fly until the best fit is obtained. Pre-computed grids of synthetic spectra with varying abundances can also be used for different sets of stellar parameters (Pérez et al. (2016)). On-the-fly synthesis has the advantage of being easily adaptable to different spectra and lines. This freedom also enables the identification of stars with unusual chemical abundances. The disadvantage is that large samples of stars must be analysed, which can take a long time. This may be particularly inefficient when the stars are very similar to one another, like those targeted by spectroscopic surveys. Ting et al. (2018) propose a method for overcoming this issue by interpolating between models.

When spectra are crowded with absorption features, as in the case of cool stars, synthesis is the preferred method. Furthermore, it is the only way to measure abundances from molecules (Roederer et al. (2014)) or very blended lines. Since we can set the wavelength region to be fitted to any size interval, abundances are not limited to being measured from individual lines with a "well-behaved" shape. The disadvantage of the spectrum synthesis method is that they are dependent on the instrumental profile (for example, the spectral resolution must be known) and each pixel is fitted, which means that the results are sensitive to an imperfect wavelength calibration.

2.5 Line broadening

A spectral line is never a monochromatic emission or absorption, it has always a width that depends on microscopic processes, macroscopic processes, and instrumental effects. Their combination causes the so-called **broadening of a spectral line profile**. This broadening can be evaluated in different ways, but the easiest and most widely used is the measure of the **Full Width at Half Maximum (FWHM)**, that is the width of the line at half of the peak over (or under) the continuum. Let us see briefly the processes that cause broadening.

Natural broadening

The energy levels of an atom are naturally broadened due to the uncertainty principle. Indeed for a level above the ground one, with energy E and lifetime Δt, the uncertainty principle states:

$$\Delta E \Delta t \sim \hbar. \tag{2.27}$$

Thus, a photon emitted with a transition that has the ground state as the final one can range within a frequency interval:

$$\Delta\nu = \frac{\Delta E}{h} \sim \frac{1}{2\pi\Delta t}. \tag{2.28}$$

The profile of the natural broadening is a very narrow **Lorentzian function**:

$$\varphi(\nu) = \frac{\frac{\Gamma}{4\pi^2}}{(\nu-\nu_0)^2 + \left(\frac{\Gamma}{4\pi^2}\right)^2}, \tag{2.29}$$

where Γ depends on the probability of natural decay of the energy levels. The Lorentzian profile is usually not detected in astrophysical spectra.

Thermal Doppler broadening

When a radiation beam at monochromatic frequency ν_0 is absorbed by a gas of particles moving at velocities v, the frequency of the absorption will be affected by the Doppler effect. Thus, the light (absorbed or emitted) is shifted according to:

$$\nu = \nu_0 \left(1 + \frac{v}{c}\right). \tag{2.30}$$

The profile, in this case, is **Maxwellian**.

Microturbulence

Microturbulence indicates a random motion of mini-cells of gas whose size is smaller than the mean free path of the photon. Microturbulence affects the absorption coefficient and modifies both the profile and the EW of spectral lines. If the mini-cells are moving according to the Maxwell-Boltzmann distribution, the broadening function has a **Gaussian shape**.

Collisional broadening

The presence of nearby particles causes collisional broadening or pressure broadening. These could be atoms, molecules, ions, or electrons. Their charge alters the radiation of the atom or ion of interest via the Coulomb interaction, which alters the frequency of a bound-bound transition between perturbed levels. These collisions are called **elastic** even though the energies are momentarily minimally changed. The word **inelastic**, instead, is designated for collisions involving bound-bound transitions between different energy levels. Collisions between atoms cannot be ignored if they are sufficiently close to each other and produce significant broadening effects.

In particular, the overwhelming numbers of neutral hydrogen atoms make them the dominant broadener of spectral lines in cool-star atmospheres. They generate the so-called **van der Waals** broadening mechanism. The collisions with charged particles such as protons and electrons, instead, generate an effect called **Stark** broadening. Finally, we have also the **resonance** broadening due to the interactions between neutral hydrogen atoms themselves.

2.5.1 The Voigt profile

Summarizing, natural and collisional broadening (Van der Waals, Stark and resonance effects) functions have a Lorentzian shape, while thermal Doppler and microturbulence broadening have a Gaussian shape. Thus, if we can combine the Gaussian and the Lorentzian profiles of the spectral line, obtaining the so-called **Voigt shape**. The core of the Voigt profile is dominated by the Gaussian, while the wings are dominated by the Lorentzian function.

2.6 Atomic models

Accurate abundance calculation requires realistic methods to compute radiative transfer. It was found that one of the main reasons for systematic uncertainties is the assumption of local thermodynamic equilibrium (LTE) instead of the more general approach of non-LTE (NLTE) (Asplund (2005)). NLTE models provide a more realistic way of treating the radiation transfer in the stellar atmosphere. The following section will focus on describing the underlying physics of this process.

2.6.1 Local Thermodynamic Equilibrium(LTE)

We consider a plasma in **thermodynamic equilibrium (TE)** when it is located in a closed system and each energy exchange process is balanced by its reverse process. The plasma is characterized by a temperature, T, and pressure, P, and emits blackbody radiation according to Planck's law. The population of the excited and ionized states follows the Boltzmann and Saha equation and the velocity distribution is **Maxwellian** (Eq. 2.31):

$$\phi(v,T) = \frac{4}{\sqrt{\pi}}(\frac{m}{2k_BT})^{3/2}v^2 \exp{(-\frac{mv^2}{2K_BT})}dv. \tag{2.31}$$

If we consider a sample of atoms and ions, we can introduce the following definitions:

- N_{in} number of i-times ionized atoms in the energy level n per unit volume (cm^{-3}),

- $N_i = \sum_n N_{ni}$ number of i-times ionized atoms in the energy level n per unit volume (cm^{-3}),
- $N = \sum_i Ni$ number of atoms and ions of an element per unit volume (cm^{-3}),
- χ_{in} excitation energy of the level n from the ground state of the i-times ionized atom (eV),
- $\chi_i = \chi_{i\infty}$ ionization energy from the ground state of the i-times ionized atom (eV),
- g_{in} statistical weight of the n level in the i-times ionized atom.

Thus, the **Boltzmann** (eq.2.32) and the **Saha** (eq.2.33) **equations** are:

$$\frac{N_{in}}{N_{i1}} = \frac{g_{in}}{g_{i1}} \exp\left(-\frac{\chi_{in}}{k_B T}\right) \tag{2.32}$$

$$\frac{N_{i+1}}{N_i} P_e = 2\frac{u_{i+1}(T)}{u_i(T)} \frac{(2\pi m_e)^{\frac{3}{2}} (K_B T)^{\frac{5}{2}}}{h^3} \exp(-\frac{\chi_i}{k_B T}) \tag{2.33}$$

where P_e is the electron pressure and u_i is the partition function:

$$u_i(T) = \sum_n g_{in} \exp\left(-\frac{\chi_{in}}{k_B T}\right) \tag{2.34}$$

A real astrophysical plasma deviates from TE, however, in many cases, it is possible to adopt the **local thermodynamic equilibrium (LTE)** approximation, which assumes that a plasma can be locally described by the previously mentioned relations. In particular, LTE is a common assumption when solving the radiative transfer problem in stellar atmospheres because it significantly simplifies the calculation of the number densities of atoms and molecules. However, in LTE conditions, the elastic collisions in which particles exchange kinetic energy are much more frequent than collisions producing excitation or ionization. The distribution of electrons is determined exclusively by particle collision processes and the latter takes place sufficiently rapidly so that the distribution responds instantaneously to any change in LTE plasma conditions. In such circumstances, each process is accompanied by its inverse, and these pairs of processes occur at equal rates by the principle of detailed balance. Thus, the distribution of energy levels of the electrons is the same as it would be in a system in complete thermodynamic equilibrium. It means that the radiation processes can be neglected with respect to the collision processes. In other words, the trouble with this assumption is that it essentially implies that stars do not radiate.

2.6.2 The non-LTE assumption

Photons and matter particles (ions, atoms, electrons, and molecules) interact in a variety of ways, including photo-excitation and ionisation, radiative recombination, stimulated emission, and others. Collisions are especially strong deep within the star, much below the photosphere, and the photon's mean free path λ is smaller than the scale over which the physical variables (temperature, pressure) change, causing the radiation field to thermalize to the Planck function. Closer to the stellar surface, λ grows larger, eventually exceeding the scale height of the material. Photons dissociate from matter as they spread outward, resulting in a non-local, anisotropic, and strongly non-Planckian radiation field.

Numerical simulations show that the radiative transition rates generated by the non-local radiation field in the outer atmospheric layers significantly outnumber collisional transition rates, and thus the populations of atomic energy levels diverge from the LTE values. Scattering causes non-locality: photons traveling through the gas change orientation randomly and experience a small frequency shift. The concept of non-LTE was developed to account for scattering in radiative transfer processes and, as a result, the formation of an element's excitation-ionisation equilibrium.

In non-LTE, the velocity distribution remains Maxwellian, while the Boltzmann and Saha equations are replaced by the rate equations or their time-independent counterpart, **statistical equilibrium (SE) equations** or kinetic equilibrium equations. The SE equation for level i, illustrated in fig. 2.5, can be written like:

$$n_i \sum_{j \neq i} P_{ij} = \sum_{j \neq i} n_j P_{ij}. \tag{2.35}$$

Here, $P_{ij} = C_{ij} + R_{ij}$ is the total of collisional and radiative rates (per particle) which establishes the equilibrium number of ions excited to the level i. A subscript ij means that a transition from the level i to the level j occurs. This equation, which represents the microscopic interaction of atoms, electrons, and photons, must be written for each level i of every ion in every unit volume of a star photosphere. To obtain the level population, **we must solve this system of equations for each level.**

It is often unnecessary to analyse each individual rate since most of them are very small and the SE is usually determined by one or two dominating channels. These channels are sequences of processes, which occur under a certain combination of factors, including the optical depth in a line or continuum, the difference between J_ν and the local Planck function, and the relative size of cross-sections for different atomic levels.

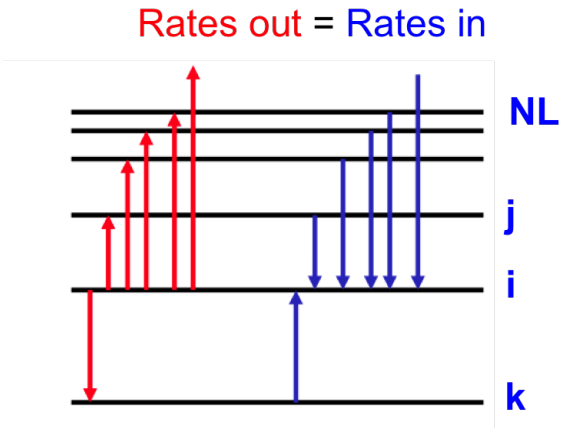

Figure 2.5: Illustration of the statistical equilibrium equation for a level i in the model atom; the sum of the rates of all transitions into a level i is balanced by the sum of the rates out. Credits: Bergemann, 2014 Bergemann and Nordlander (2014).

Why is the NLTE assumption so important in astrophysics?

Many investigations have discovered that NLTE effects significantly impact the computation of chemical abundances in stars. Knowing the effects of the NLTE, it is easy to determine the behaviour of the optical lines. Predicting more realistic absorption line profiles means providing more accurate stellar parameters and abundances. The NLTE mechanisms that affect atoms' behaviour are well described by Bergemann and Nordlander (2014) and Rutten et al. (1995) and are displayed in the following.

- **Over-ionisation and photon pumping.** A super-thermal radiation field with mean intensity larger than the Planck function, $J_\nu > B_\nu(T_e)$, leads to over-ionisation (Fig. 2.6a) and over-excitation (Fig. 2.6d), or photon pumping. In a typical stellar atmosphere, the mean intensity in the continuum $J_{\nu,c}$ is significantly higher than the local Planck function blueward of the stellar flux maximum. Thus, over-excitation and over-ionisation affect the neutral atoms, which have ionisation thresholds in the blue and UV.

- **Over-recombination.** If the mean intensity is lower than the Planck function, $J_\nu < B_\nu(T_e)$, the shortage of ionisations leads to the net over-recombination to the upper levels (Fig. 2.6b), as is the case in the infrared (Fig. 3, bottom panel). Over-recombination takes place in the bound-free transitions with the corresponding wavelengths; this is the case for the majority of neutral atoms (NaI, KI, CrI, FeI, etc).

- **Photon "suction".** It is a sequence of spontaneous transitions caused by photon loss, in the atmospheric layers where the line centre optical depth has

dropped below unity for every transition involved in the sequence (Fig. 2.6c). Such a sequence can include transitions of various frequencies, from UV to IR. Photon suction is balanced by the recombination flow through the bound-free edges in the IR.

- **Photon loss and resonance line scattering.** If the optical depth falls below unity in a line, $\tau_{\nu_0} < 1$, the photons escape without reconversion to thermal energy. This is termed photon loss. In the framework of statistical equilibrium, radiative excitations are in deficit, and spontaneous deexcitations lead to the over-population of the lower level in a transition out of the upper level (Fig. 2.6c,e,f). The effect is particularly important for strong resonance lines with very small collisional destruction probability: photon escape in the line itself influences the line source function, causing sub-thermal s_ν.

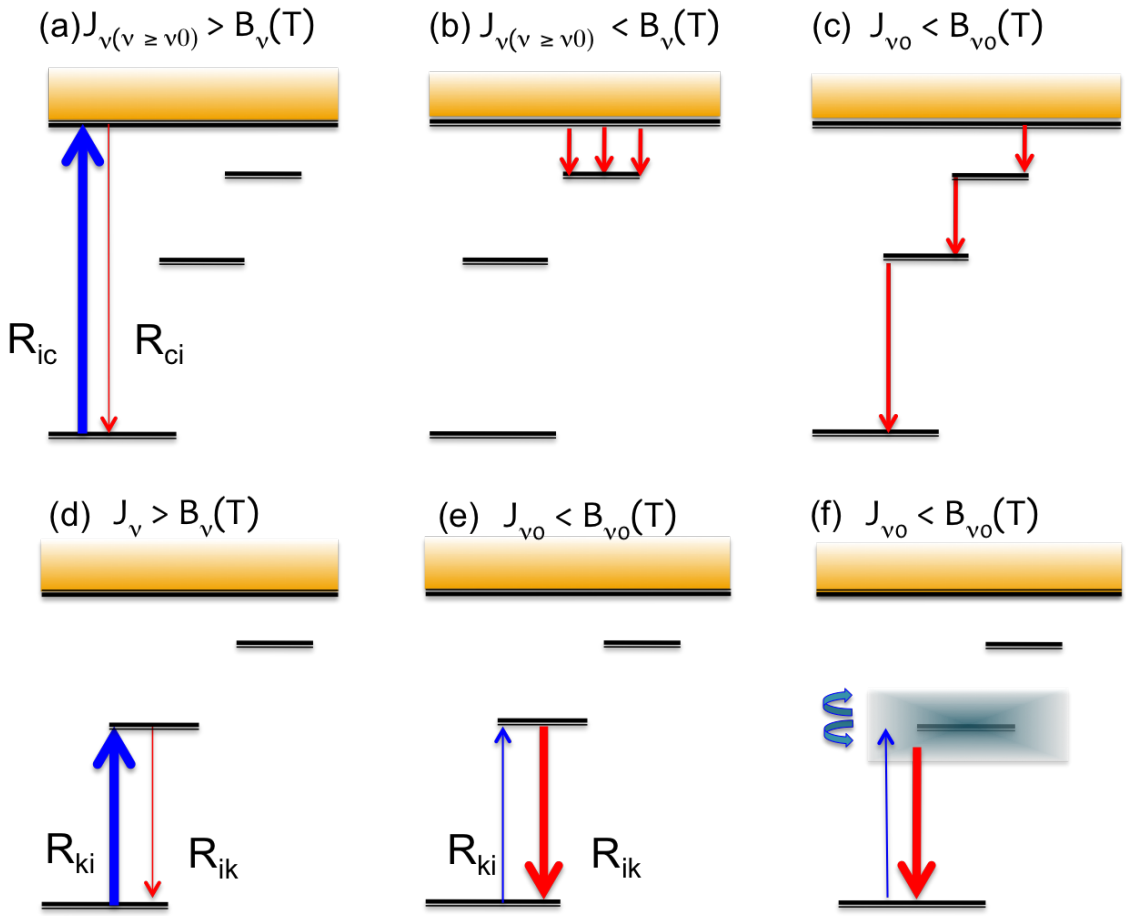

Figure 2.6: Illustration of reaction channels for a hypothetical multi-level atom. ν_0 is the central frequency for a spectral line or the frequency of ionisation threshold. Credit: Bergemann and Nordlander, 2014Bergemann and Nordlander (2014)

Chapter 3

Copper atom

As already mentioned, nowadays spectroscopic studies are becoming increasingly important. The understanding of the chemical evolution of our Galaxy, as well as the discovery of the nucleosynthesis processes in the universe, are the major goals of precision spectroscopy. In this context, it is very useful to study the atoms one by one, by developing precise atomic models. From these, by modeling the stellar atmosphere, the radiative transfer processes, and having the atomic data calculations, the chemical compositions of the stars can be retrieved.

The aim of my thesis was to produce a complete model atom for copper, of which the Grotrian diagram is presented in fig.3.1, that will be used in the future by the stars' research group of Stockholm University and their collaborators to try to solve some open questions in astrophysics. Cu is of particular interest among the iron-peak elements because the astrophysical site for Cu synthesis is not yet well established (Sneden et al. (1991); Mishenina et al. (2002); Bihain et al. (2004)). The study of [Cu/Fe] in stars of various metallicities provides an important indication of the nucleosynthetic processes derived from the progenitor stars that contribute to the formation of this element. This information is crucial because Cu is thought to be synthesized by several possible nucleosynthesis scenarios, and yet the contributions of these scenarios are still in dispute. Moreover, the abundance of copper plays an essential role in the investigations of the chemical evolution of various stars, such as giant stars (McWilliam and Smecker-Hane (2005)). Finally, it has a unique evolutionary trend as the [Fe/H] varies from extremely metal-poor to solar abundance. The causes of this behaviour must be verified. In the next subsections, I reported a summary of what are the most important reasons for studying copper with some practical examples of open problems in astrophysics regarding Cu.

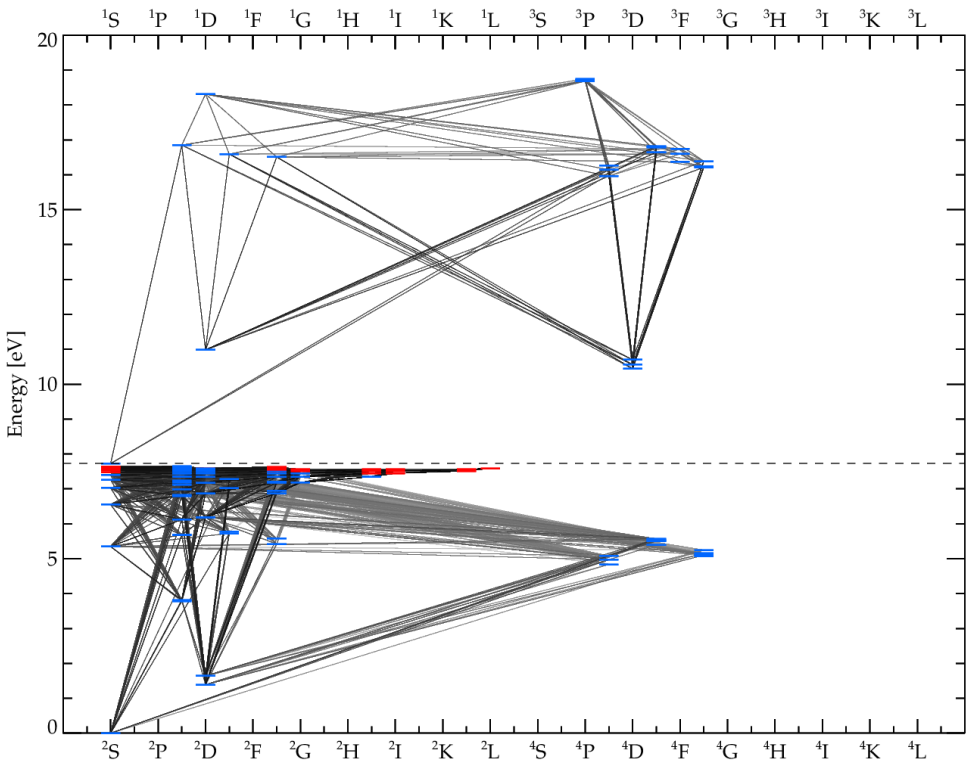

Figure 3.1: Grotrian diagram of the reduced atom showing the energies for possible bound-bound transitions of Cu I (lower half) and Cu II(upper half). Transitions are shown by black lines, with darker lines representing a higher oscillator strength. Blue marks show the observed energy levels, and red marks show levels that are theoretically predicted. Credits: Karin Lind.

3.1 Copper nucleosynthesis

The process of creating new atomic nuclei, the protons and neutrons that make up an atom's center, is known as nucleosynthesis. Within a few minutes after the Big Bang, the process of nucleosynthesis began. Protons and neutrons were created at that time from a quark-gluon plasma, a mixture of quarks and gluons. The neutrons and protons combined to form the deuterium, an isotope of hydrogen, nuclei after the universe slightly cooled. The resulting fusion of deuterium nuclei produced helium. Lithium was created through additional interactions between protons, neutrons, and various helium isotopes. The hydrogen and helium produced during this phase of the universe eventually created the universe's first massive stars. Since then, the majority of the other nuclei in the universe have been formed through nuclear reactions during the birth and death of stars. Stars can produce nuclei in one of two ways: either by fusing two smaller nuclei together (a process known as fusion)

or by shattering a larger nucleus into several smaller nuclei (called fission). New atoms are created in both cases. The elements on the Periodic Table that we are familiar with today were also created in the past by these processes. Different types of stars generate nuclei made of various elements, which eventually led to a variety of natural elements.
The first stars in the universe were huge, frequently exceeding ten times the size of the Sun. They also lived much shorter lives than more recent stars. They produced the elements in the Periodic Table up to iron by burning hydrogen while they were alive. These elements' nuclei were expelled from them when they died in an explosion known as a core-collapse supernova. Neutron stars can be left behind by supernovae. When neutron stars merge, they produce new nuclei, including elements that are heavier than iron. Other stars become white dwarfs as they die. These white dwarfs may also merge and synthesize nuclei of elements.

In this complicated panorama, it can be very difficult to discern the nucleosynthesis processes of heavier elements. Indeed, despite numerous investigations on stellar nucleosynthesis, the scenario for copper creation in stars remains enigmatic. It is still contested whether copper is formed mostly in massive stars or Type Ia supernovae. Sneden et al. (1991) discussed potential mechanisms for copper synthesis in stars in the wake of their high-resolution observations (which revealed a decline in [Cu/Fe] with decreasing [Fe/H] in Galactic stars) and supported a secondary origin for Cu through the weak component of the s-process in massive stars. However, according to Raiteri et al. (1993), the primary s-process which takes place in the low-mass asymptotic giant branch (AGB) stars, does not contribute more than 5% to the synthesis of Cu isotopes. Moreover, the work by Raiteri et al. (1993) also states that only 25 % of solar Cu was attributed to the weak s-process in massive stars, while Matteucci et al. (1993) hypothesized that most solar Cu originated in Type Ia supernovae (SNe Ia). Current SN Ia models, however, predict a negligible production of Cu during thermonuclear explosions (Iwamoto et al. (1999), Travaglio et al. (2004). It has been recently claimed that up-to-date, high-resolution spectroscopic data for solar neighbourhood stars belonging to different Galactic substructures (halo, thick disc, and thin disc), bulge-like stars, globular clusters (GCs) and dwarf spheroidal galaxies (dSphs) can all be well understood if Cu is mostly a secondary product of massive stars, with a small primary contribution from explosive nucleosynthesis (Bisterzo et al. (2010)). Also, Romano and Matteucci (2007), concluded that, after a short phase in which the primary contribution from explosive nucleosynthesis in core-collapse SNe dominates, the evolution of Cu in galaxies is regulated mostly by the weak s-process occurring in massive stars. And even if it seems the most likely scenario, some other studies to confirm have to be done. For all the above-mentioned reasons, copper looks like a very intriguing element. Moreover, of the aforementioned studies, some were performed by assuming LTE, others by using

NLTE models. This aspect requires further investigation.

3.2 The NLTE mechanism in Cu atom

In section (2.6.2), I presented all the NLTE mechanisms that can affect atoms. According to Shi et al. (2014) and Yan et al. (2015, 2016), the deviations from LTE in Cu I is due to **UV overionization**. Overionization implies that

$$n_i P_{ij} - n_j P_{ji} > 0 \tag{3.1}$$

where n_i is the level population of a bound state of a neutral atom and n_j is the ground state of the ionized atom. Pij are defined, like in the previous section, as $P_{ij} = C_{ij} + R_{ij}$ where R_{ij} is the radiative rate from level i to j and C_{ij} is the corresponding collisional rate. In other words, overionization means that the ionization–recombination balance for a transition is shifted towards more efficient ionization, which tends to depopulate the lower level with respect to LTE.
In Fig. 3.2, I present how the departure coefficients ($b_i = n_i^{NLTE}/n_i^{LTE)}$)of all the levels of Cu I and Cu II vary with the continuum optical depth at 5000 Å $\log(\tau_{5000})$ for the model atmosphere of the Sun, where b_i is the ratio of the number density of non-LTE (n_i^{NLTE}) to that of LTE (n_i^{LTE}). The decision to take the optical depth at 5000 Å is purely conventional since it is roughly the peak of the solar blackbody and it also falls in the visible part of the spectrum. $\log(\tau_{5000}) = 0$ is equal to $\tau_{5000} = 1$ and corresponds to the surface of a star. At this point, most of the light can freely escape the atmosphere. Then, the deeper you go into the star (bigger values of $\log(\tau_{5000})$, the higher the density and the closer you get to LTE. Indeed, higher densities mean a higher collisional rate. On the other hand, going the opposite way, the further out of the star, the lower the density. In this case, radiation becomes important and NLTE effects become stronger. From this plot, the presence of overionization becomes much more clear. Indeed, most of the lines of Cu I (in red) are below the black line that represents $b_i = 1$ (condition for LTE). This happens because the population of Cu I levels is greater if calculated in LTE than in NLTE, due to the overionization which empied the levels of Cu I. As a consequence, the ratio b_i for Cu I becomes lower than 1. On the other hand, the departure coefficients of Cu II are larger than 1, since the neutral copper levels are largely populated. The plot also shows that the NLTE mechanisms begin to underpopulate the outside layers from $\log(\tau_{5000}) = -1$ due to overionization.

According to Shi et al. (2014), for the solar Cu I lines, the departures from LTE are small with the mean NLTE abundance correction of ≈ 0.01 dex. However, Korotin et al. (2018) checked the consistency between the copper abundance derived in six metal-poor stars using UV Cu II lines (which they assumed to be formed in LTE) and UV Cu I lines (treated in NLTE). They reported that the NLTE

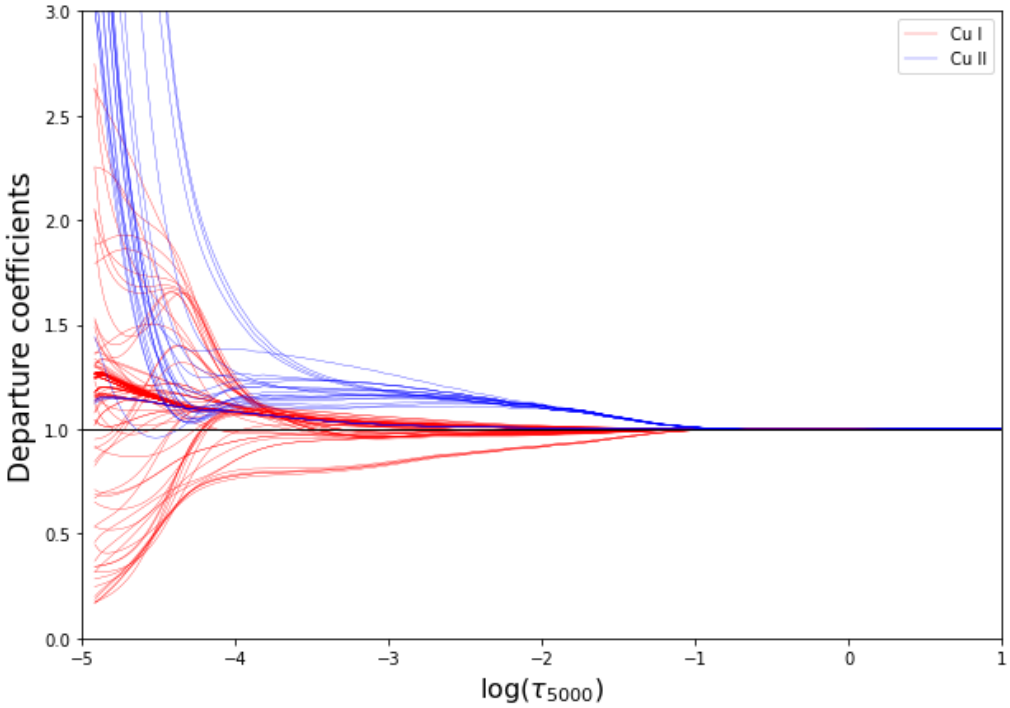

Figure 3.2: Departure coefficients of Cu I in red, in and Cu I in blue

corrections are close to zero for the stars of solar metallicity and quickly increase for the metal-poor stars. The result is shown in Fig. 3.3.

All in all, a NLTE calculation is needed in order to infer the correct Cu abundance.

3.3 Copper abundances in Omega Centauri

The idea of working on the construction of this atomic model was born thanks to our interest in the peculiarity of **Omega Centauri**. It is the most massive globular cluster of the Milky Way. It contains approximately 10 million stars and has a total mass of around 4 million solar masses (Baumgardt and Hilker (2018)). Due to the large star-to-star metallicity variations, some authors speculated that Omega Centauri is the naked nucleus of a dwarf satellite galaxy captured into a retrograde Galactic orbit many billion years ago. It is now widely accepted that Omega Centauri hosts at least 17 distinct stellar populations with different abundances of some light elements (including He, C, N, O, Mg, Al, Si, Na, and K), iron, and s-process elements. The multiple stellar populations are clearly visible via photometric studies

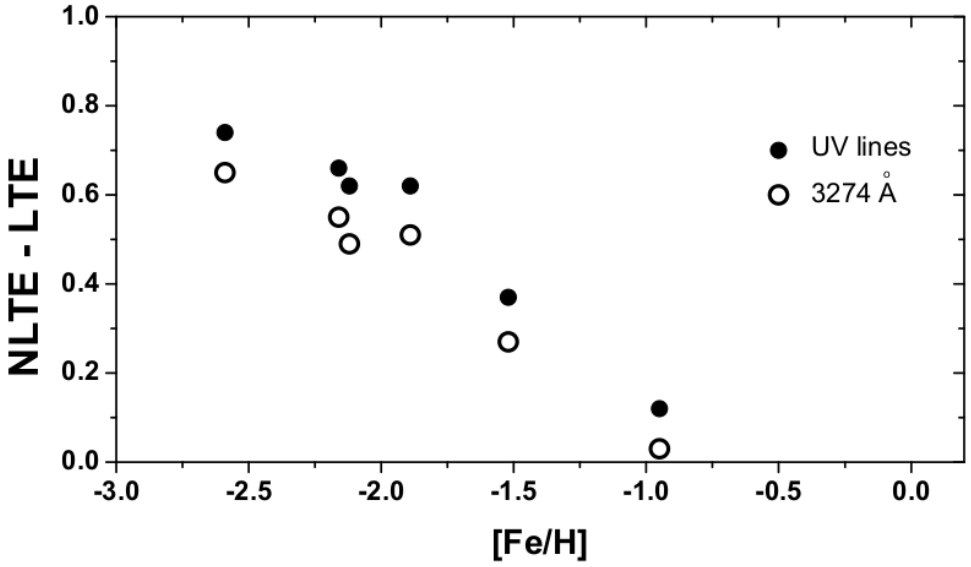

Figure 3.3: Non-LTE corrections to the LTE copper abundances calculated for Cu i UV lines and 3274 Å as a function of [Fe/H]. Credits: Korotin et al. (2018)

as distinct sequences in the color-magnitude diagram (CMD) and in other diagrams.

The [Cu/Fe] ratios seem to confirm the connection between Omega Centauri and a dwarf galaxy. Indeed [Cu/Fe] generally shows a decreasing trend in the low-metallicity region in Galactic stars, but this does not happen in the stars of the globular cluster Omega Centauri. The only other systems known to have unusually low [Cu/Fe] ratios are the Sagittarius dSph (McWilliam and Smecker-Hane (2005)) and the Large Magellanic Cloud (Pompéia et al. (2005)). In particular, the finding of the similarity between the Cu values of Omega Centauri and Sagittarius, which is tidally shattered and merging with the Milky Way, lends support to the idea that the halo of the Galaxy has been formed, at least in part, by the accretion of comparable dwarf systems. Moreover, it suggests that the two systems followed similar chemical enrichment histories, thus supporting the idea that Omega Centauri is the surviving nucleus of an accreted dwarf galaxy.

However, so far, spectroscopic studies of copper abundance in Omega Centauri have only been performed in LTE approximation, which is not suited in this case, since we know that the Cu I lines formation is affected by NLTE mechanisms and that the NLTE corrections become relevant at lower metallicities.

Chapter 4

Atomic model

4.1 Atom overview

In the first part of my thesis work, I assembled a new model atom for Cu I and Cu II, operating the state-of-the-art 3D non-LTE radiative transfer code Balder (4.3). The atom was developed considering bound-bound radiative transitions, photo-ionisation cross-sections, hydrogen collision rates, and electron collision rates. The rate coefficients encompass all collisional and radiative transitions for ionisation, de-excitation, and charge transfer, the reverse of which being calculated internally in Balder. Along with the energy of each level, the atom also carries information about the level's statistical weight, valence electron configuration, and ionisation status. The oscillator strength of the transition, which serves as a representation of the likelihood that the absorption will take place, can be found in bound-bound radiative transitions.
The total number of wavelength points that can be employed to keep processing power and time at a tolerable level is restricted, therefore they also contain the resolution needed for the observed line. Additionally, it features data to model the aforementioned line widening (see chapter 2.5).
Since the electron is impacted by a range of photon frequencies, not just at a discrete value, the radiative ionisation requires a wide range of photon energies and their rate coefficients. Moreover, as a higher temperature increases the kinetic energy of the environment and particles, raising the collisional rate coefficients, the collisions also need to contain collisional information at various temperatures. However, it has been found that temperature has a significant impact on excitations, but not on the opposite transitions of de-excitations.

4.1.1 Data

The energy levels and bound-bound transition data were taken from the spectroscopic line calculation performed by Kurucz (1999). The atom contains 150 energy

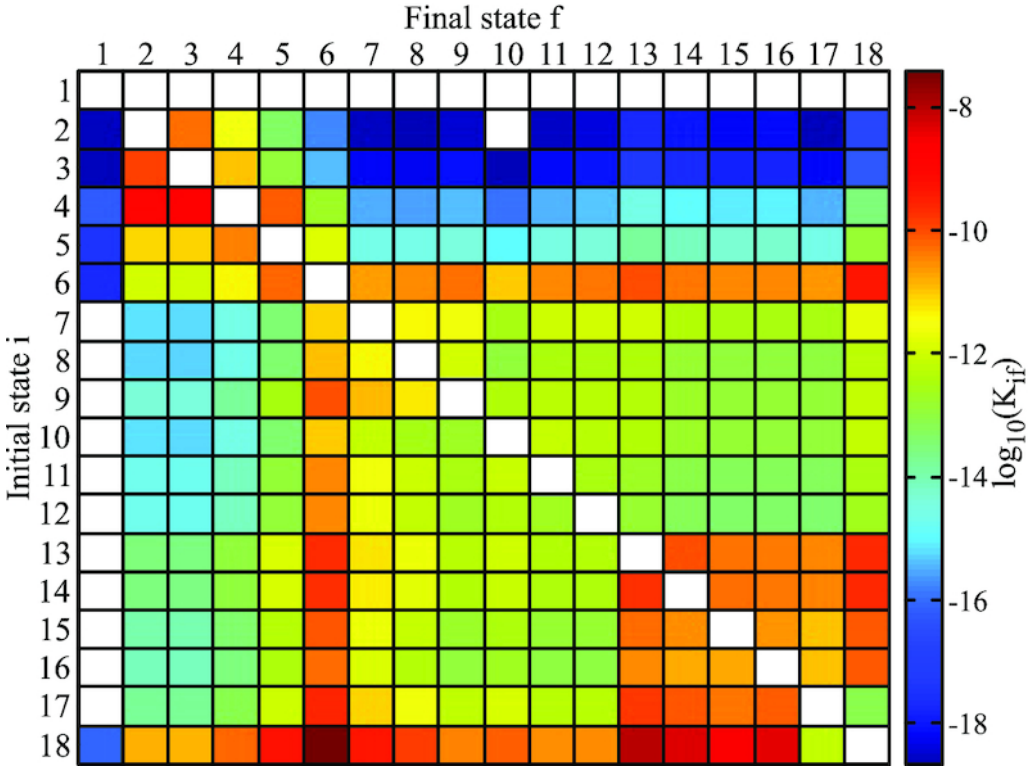

Figure 4.1: Collisional rate for $Cu+H$ and $Cu^{+}+H^{-}$ collisions at T=6000K. Credits Belyaev et al. (2020)

levels: 125 belonging to Cu I and 25 to Cu II. The photo-ionisation cross-sections were calculated by Liu et al. (2014). Their calculations were carried out in the LS-coupling scheme by using the R-matrix program, which is a modified version of the Belfast atomic R-matrix program RMATRX1. Then, I considered the hydrogen collisions data recently published by Belyaev et al. (2020), calculated taking into account the fine structure effects in inelastic collisions for many-electrons case. In fig 4.1 is shown a graphical representation of the rate coefficients for the partial processes of excitation, de-excitation, neutralization, and ion-pair formation in $Cu+H \leftrightarrow Cu^{+}+H^{-}$ collisions, at temperature T=6000 K. However, the model was built taking into account transitions between states calculated for the temperature range from T=1000 K to T=10000 K.

The electron collisions rates were computed with a semi-empirical recipe since there were no available data in the literature. To do that I used the formulae provided in Allen's astrophysical quantities (Cox (2000)), for which the formalism is given in the following section.

Van Regemorter formalism

These formulae, previously discussed by Van Regemorter, reveal that the classical cross-section of atoms for ionization by an electron is:

$$Q_i = 4n\pi a_0^2 \frac{1}{\chi\epsilon}(1 - \chi/\epsilon) \tag{4.1}$$

where χ is the ionization energy in rydbergs (Ry), ϵ is the electronic energy before collision in Ry, and n is the number of optical electrons. The general approximation for the cross-section of atoms for ionization by electrons is:

$$Q_i = n\pi a_0^2 \frac{1}{\chi\epsilon} F(Y, \epsilon/\chi) = \frac{n\pi a_0^2}{\chi^2} q = 1.63 \times 10^{-14} n(1/\chi_{eV}^2)(\chi/\epsilon)F(Y, \epsilon/\chi) \tag{4.2}$$

where Y is the charge on the ionized atom (or next ion stage) and χ_{eV} is the ionization energy in eV. The function $F(Y, \epsilon/\chi)$ is given and q is the reduced cross-section. Y has been derived from experiments.
For the classical case, the maximum ionization cross section is:

$$Q_{max} = n\pi a_0^2 \chi^{-2} \tag{4.3}$$

where we substituted $\epsilon = 2\chi$ in 4.1.The value of Q_{max} is approximately the same in actual case but occurs near $\epsilon = 4\chi$. The rate of ionization by electrons is:

$$L_i = \overline{(vQ_i)} \tag{4.4}$$

Where v is the Maxwellian velocity distribution.

Also, the approximation for the excitation cross section of an atom $[cm^2]$ (for allowed transition) is given:

$$Q_{ex} = \frac{8\pi}{\sqrt{3}} \pi a_0^2 \frac{f}{\chi\epsilon} b = \frac{n\pi a_0^2}{\chi^2} q = 1.28 \times 10^{-15} n(f/\epsilon W)b \tag{4.5}$$

where f is the oscillator strength, W is the excitation energy in Ry and ϵ is the electron energy before collision in Ry. b is given.
The maximum excitation cross-section is as follows:

- the neutral atom approximation gives

  $$Q_{max} = 125\pi a_0^2 \lambda^2 f \tag{4.6}$$

  near $\epsilon = 3W$

- the ion approximation gives:

$$Q_{max} = 350\pi a_0^2 \lambda^2 f \tag{4.7}$$

  near $\epsilon = W$

The rate of excitations by electron collisions is:

$$L_{ex} = \overline{(vQ_{ex})} = 17.0x10^{-4} \frac{f}{T^{1/2} W_{eV}} 10^{-5040 W_{eV}/T} P(W/kT) \tag{4.8}$$

where W_{eV} and W are the excitation energy in eV and in ergs and P(W/kT) is tabulated.
Also, the deexcitation cross-section can be retrieved by relating them with the excitation cross-section. Being 1 the lower level and 2 the upper:

$$g_2 \epsilon_2 Q_{21} = g_1 \epsilon_1 Q_{12} \tag{4.9}$$

where $\epsilon_2 = \epsilon_1 + W$ and g_1 and g_2 are the statistical weights.
The deexcitation rate L_{21} and excitation rate L_{12} are related by:

$$g_2 L_{21} = g_1 L12 \exp(W/kT) \tag{4.10}$$

Finally, these formulae allow us also to calculate the excitation cross sections for forbidden transitions. In this case, the collisional strength Ω for each line is defined by:

$$Q_f = \pi \Omega / g_1 k_\nu^2 = \pi a_o^2 \Omega / gi\epsilon = \frac{h^2 \Omega}{4\pi m^2 g_1 v^2} = 4.21 \Omega / g_1 v^2 \tag{4.11}$$

where $k_\nu / 2\pi$ is the wave number of the incident electron, ν in the electron velocity, g_1 is the statistical weight of the initial (lower) level, and Q_f is the cross-section of the forbidden line for atoms in this level. Then it is valid: $\Omega_{12}(excitation) = \Omega_{21}(de - excitation)$.

The formalism expressed above was implemented using an application of Balder called NEWCOL. In fig. 4.2 are illustrated the results I obtained with the formulae above. The rate coefficients (cm^3/s) are plotted as a function of the energy difference of each transition (cm^{-1}).

4.1.2 The hyperfine structure and isotopes

In spectroscopy, hyperfine structure (HFS) is the splitting of a spectral line into a number of components due to energy changes produced by electron spin–orbit

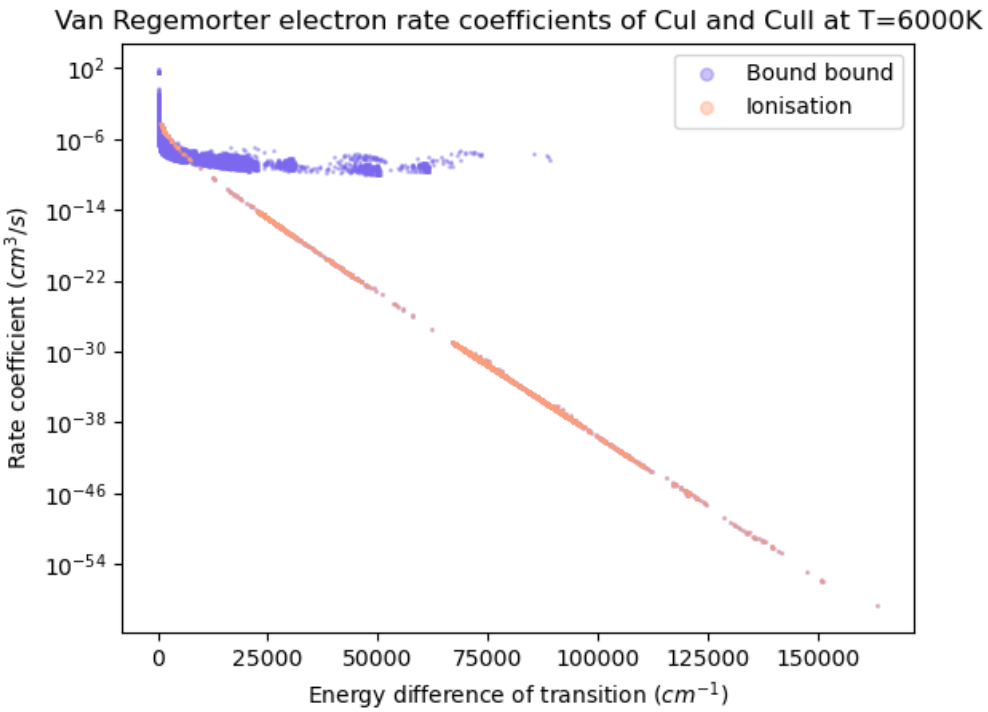

Figure 4.2: Rate coefficients of ionization (pink) and excitation (blue) by electrons of CuI and CuII

coupling. Indeed, the contribution of the rotation of the electrons around the nucleus should be added to the one of the atomic nucleus itself which spins about its own axis. A similar effect of line splitting is caused by mass differences (isotopes) of atoms in an element and is called isotope structure, or isotope shift. These spectral lines, which are also known as hyperfine structures, can be seen in an element with isotopes with spin zero.

Copper is an s-process nucleus with two stable isotopes: ^{63}Cu and ^{65}Cu. The isotopic fraction between the two was assumed to be 0.69 and 0.31, respectively (Asplund et al. 2009). There are two different isotope effects, the **mass effect** and the **volume effect**. In the first case, the effect is to displace the centre of mass between the nucleus and electrons by a small amount. Obviously, the shifts would be greatest for very light atoms, while would be negligible for heavier atoms. Thus, for example, the hydrogen atom is largely affected by the mass effect, while the iron is not. However, heavy atoms are mainly affected by the volume effect, which is related to the penetration of the nuclei by s-electrons. The electric charge distribution of the nucleus changes as a result of this volume discrepancy. Using a simplified model, the difference in an energy level brought on by a volume difference

can be calculated as the mean-square difference in charge radius multiplied by the change in the total electron probability density at the origin. Following Shi et al. (2014), we added HFS and isotopes' contribution to twelve lines in the atomic model. The hyperfine structure (HFS) components of the line transitions were computed based on the Russell–Saunders coupling method. They adopted the log gf values from Kono and Hattori (1982), Kock and Richter (1968), and Carlsson (1988), while the van der Waals damping constants ($\log C_6$) for Cu I lines are calculated according to the Anstee and O'Mara (1991, 1995) tables. These last values are very important for Cu I strong lines in dwarf stars. All the above-mentioned parameters needed to determine the copper abundance for the selected lines are presented in Table 1 of Shi et al. (2014). They combine all components within 1 Å if the HFS components of the lines fall into more small intervals. The synthetic NLTE profiles with and without HFS for the line of Cu I at 5700 Å in the solar flux spectrum are shown in Figure 4.3.

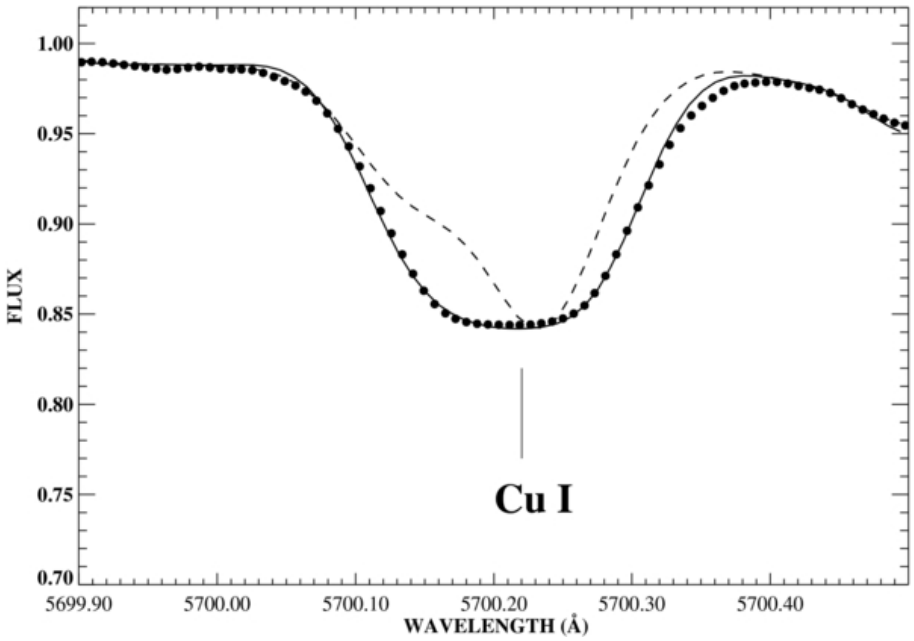

Figure 4.3: Synthetic NLTE profiles with (solid line) and without HFS (dashed line) for the line of Cu i at 5700 Å in the solar flux spectrum. Credit: Shi et al. (2014)

4.2 Atom reduction

In the previous sections, I reported how the comprehensive model for Cu was constructed. Taking into account all the contributions, we obtained an atom with

hundreds of levels and hundreds of thousands of radiative transitions. This configuration makes the NLTE calculation feasible, even in 1D. Thus, to reduce the computational time, the number of frequency points for bound-bound and bound-free radiative transitions was reduced by merging similar energy levels into superstates. Even though this is a large reduction, there would still exist many transitions, and the reduction does not have a significant impact on the final result (Lind et al. (2017)). Moreover, the photoionisation cross-sections were interpolated onto a common wavelength grid with fixed logarithmic steps, reducing again the number of unique wavelength values. It allowed our radiative transfer code Balder (4.3) to treat each set of identical wavelength values as a single one during the run.

4.3 Balder

To generate the synthetic spectra I used a 3D non-LTE radiative transfer code called **Balder** (Amarsi et al. (2019)). It is originally based on the code **MULTI3D** (Botnen and Carlsson (1999)), but with some upgrades integrated by our collaborators. This chapter is devoted to providing a brief overview of the code.
Balder employs the **MALI** algorithm (Rybicki and Hummer (1991)) to solve the equations of statistical equilibrium together with the radiative transfer equation on short characteristics, assuming no feedback on the background atmosphere. The mean radiation field is determined by solving the radiative transfer equation using a short characteristic integral solver (Ibgui et al. (2013)), using the eight-point Lobatto quadrature on the interval for the integration over $\mu = cos\theta$, where θ is the angle relative to the vertical, and, for non-vertical rays, an equidistant four-point trapezoidal quadrature on the interval for the integration over the azimuthal angle ϕ.
Another important tool implemented in Balder is **Blue** (Amarsi et al.2016b). It was used within Balder to determine the equation-of-state (EoS) and the background opacities for around 10^6 lines from atomic and ionic species and 10^8 lines from molecular species. EoS are calculated using the Saha-Boltzmann equation (LTE) but with some corrections for Debye shielding. This is a process due to the interaction of charged particles with the electric field of other charged particles. The correction is implemented by reducing the ionization potentials. The bound-free (continuous) opacities were inferred on-the-fly, while the bound-bound (line) opacities were pre-computed for different temperature-density-metallicity combinations, and interpolated at runtime. Care was taken not to double-count opacities already included in the model atoms.

4.3.1 Model of stellar atmosphere

In Balder, we can use different stellar models both in 1D and 3D. These two are very different in the assumption they use. The one-dimensional (1D) model atmosphere is actually represented by a sizable table that lists the gas temperatures, pressures, and a variety of other characteristics as they change with depth from the stellar surface. It is common practice to use one-dimensional theoretical codes to simulate the atmospheres of stars while assuming solar or scaled-solar chemical composition. Based on each star's unique chemical makeup and the sporadic presence of strong magnetic fields, line opacity in these stars differs significantly from that of typical stars and also varies significantly from one star to another. One of the main problems of the 1D models' atmosphere, is the treatment of surface convection. The classical mixing-length theory (Böhm-Vitense (1958)), a parameterization designed to get around the lack of a rigorous mathematical formulation for the convective energy transfer, is typically used to compute the convective energy transfer. However, because it disregards the convective phenomena' adiabatic cooling and time dependence, this parameterization provides a poor description of these mechanisms. In 1D modelling, there are two types of photospheric turbulent motions based on the size of the turbulent element: microturbulence and macroturbulence. Microturbulence is defined as having a turbulent element that is smaller than the mean free path of the photons. If it is larger, we have macroturbulence. These motions broaden the spectral lines. In 1D model, the convective motions on the stellar surfaces are described by setting the microturbulence velocity as a fixed parameter.

A more realistic representation of the convective motion is given by the 3D models. The atmosphere of a cool star like the Sun is governed by overturning convective flows, pulsating waves, rotating tornados, and small-scale turbulent motions. Figure 4.4 shows the light intensity of a tiny patch of the solar surface: bright granules bring hot material from the stellar interior up to the surface, where it cools down and sinks back into the dark intergranular lanes. Just like stationary 1D model atmospheres, dynamical 3D models are used to analyse observed stellar spectra, allowing in addition to studying the effects of temperature fluctuations and motions.

During my work, I investigated Copper abundance in the Sun using a 1D model atmosphere since it has been more convenient in terms of computational time. Of course, one next step could be to use a 3D model.

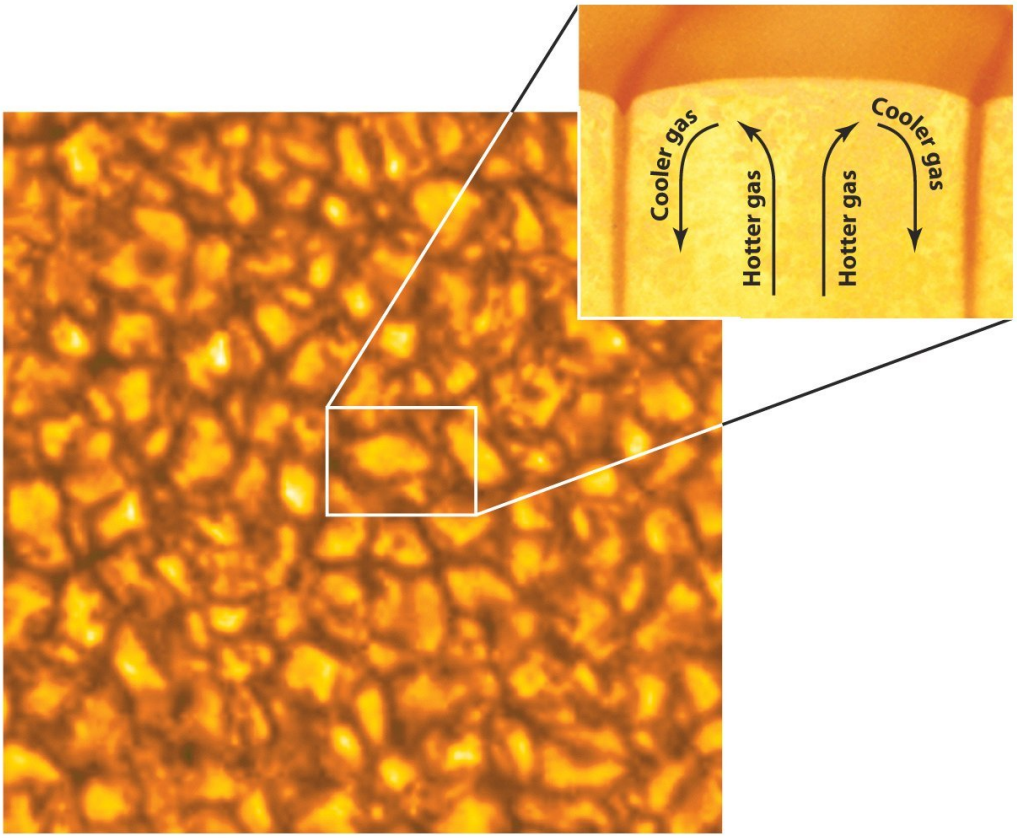

Figure 4.4: Granules on the photosphere of the Sun are produced by convection currents of plasma within the convective zone of the Sun (thermal columns, Bénard cells). Granulation, caused by the tops of these convective cells, is what gives the solar photosphere its granular appearance. In the centre, where the plasma is hotter, the granules rise to the surface. Due to the cooler descending plasma, the granules' outer edge is darker. Doppler shift measurements of the light from individual granules provide evidence for the convective nature of the granules in addition to the visible appearance, which would be explained by convective motion. A typical granule lasts 8 to 20 minutes before dissipating and has a diameter of about 1000 km. Credit: spaceplasma.com

Chapter 5

Results

5.1 Copper lines in stellar spectra

For more information on nucleosynthesis and stellar yield during galactic evolution, it is crucial to comprehend the line formation of copper nuclei in cool stars. The copper nucleus is primarily an s-process nucleus with two stable isotopes. Cu production at low metallicities may result from a variety of nucleosynthetic processes (Pignatari et al. (2010).) As we said many times, the scientific importance in studying the abundance of Cu is because the astrophysical site for the synthesis of Cu is still enigmatic, and the study of [Cu/Fe] in stars of different metallicities gives an important indication of the nucleosynthetic processes derived from the progenitor stars that contribute to the formation of this element.

For studying copper we first need to select the most reliable absorption lines. Historically, observations of copper abundances rely mostly on Cu I optical lines. The strongest line in the near-infrared was used by Prochaska et al. (2000) for their observations of copper abundances; meanwhile, Bihain et al. (2004) and Cohen et al. (2008) used the resonance lines at the UV region. They discovered that [Cu/Fe] versus metallicity ([Fe/H]) exhibits almost solar behaviour for [Fe/H]> -1 and then decreases to a flat value with [Cu/Fe]~ -1.0 at [Fe/H]< -2.5. For stars with [Fe/H]> 1.0, we can use several absorption lines to determine the copper abundances; however, this is not the case for metal-poor stars with [Fe/H]< -1.5. The situation is even worse for hot turnoff stars with effective temperatures between 6200 and 6500 K. Cu I is almost completely ionised in these types of stars, leaving no neutral copper atoms in the excited levels. The two strongest optically Cu I lines, located at 5105 Å and 5782 Å in giant stars, as well as the resonance lines, located at 3247 Å and 3273 Å in both dwarf and giant stars, are the only reliable indicators of Cu abundance. The resonance lines' strength and ability to remain measurable at low metallicities is an advantage. Bihain et al. (2004) have been able to measure the

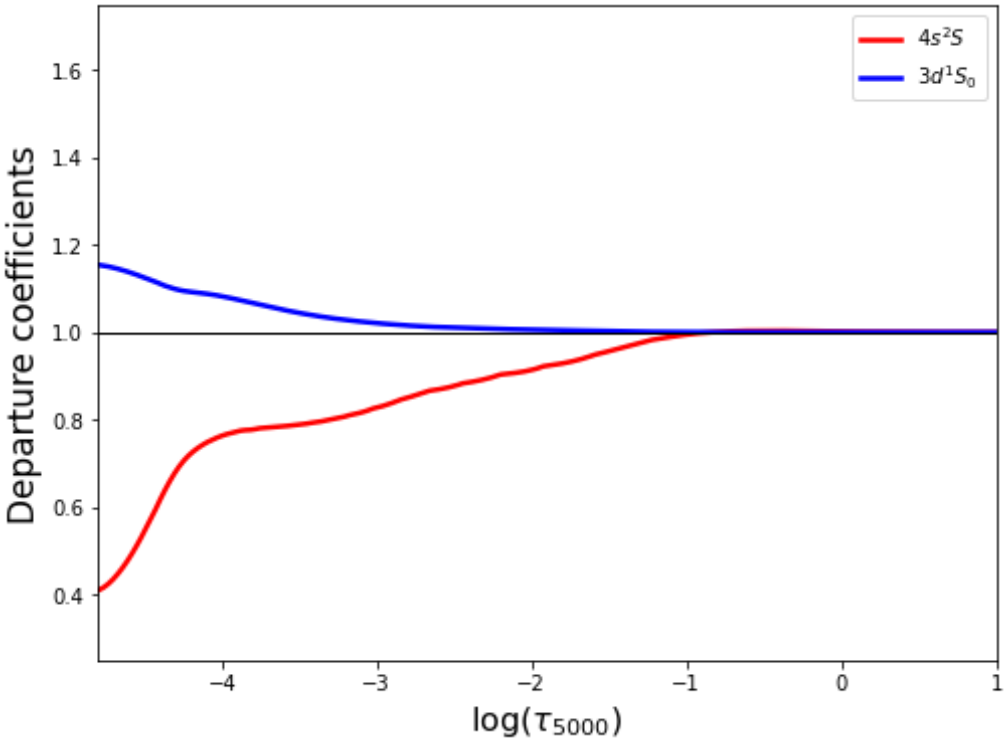

Figure 5.1: $b_i(N_i^{NLTE}/N_i^{LTE})$ as a function of $\log(\tau_{5000})$ for our final Cu atomic model for the ground states of Cu I and Cu II. The plot with the departure coefficients of all the states is presented in Fig. 3.2. In both cases, the populations of the level computations were initially performed with a copper abundance of $\log_{\epsilon_\odot}(Cu) = 4.19$. However, it was found that departures from LTE do not depend much on the exact value of the used copper abundance.

3273 Å line in the extremely metal-poor dwarf G64-12 ([Fe/H] ~ -3). These two lines are located in a spectral range that is challenging to observe for cool stars due to the lower UV flux. Moreover, they are heavily blended by other metal lines, particularly for metal-rich stars. For these reasons, abundance derivations with these two strong lines are hampered. A careful line synthesis must take into account all of the blend lines. However, some local thermodynamic equilibrium (LTE) analysis, covering a wide range of metal abundances, can be found from solar to metal-poor halo stars, like the traditional analysis of solar copper abundance by Kock and Richter (1968) and Sobeck et al. (2005). Kock and Richter (1968) calculated the solar Cu abundance to be $\log_{\epsilon_\odot}(Cu) = 4.16 \pm 0.08$ based on six optical lines, but Sobeck et al. (2005) discovered that the $\log_{\epsilon_\odot}(Cu)$ value of the line at 5105 Å is more in line with the standard value: $\log_{\epsilon_\odot}(Cu) = 4.21$. Recently, Bonifacio

et al. (2010) discovered that the Cu I resonance lines are not accurate abundance indicators after performing three-dimensional line formation with hydrodynamical models for Cu lines in metal-poor stars. They suggested that to properly describe these lines, the departure from LTE should be considered. And in order to calculate the Cu abundances for extremely metal-poor stars, we must rely on the resonance lines at 3247 and 3273 Å. It should be noted that atomic interaction processes cause the ground state to be either over- or under-populated, which will cause systematic errors for an LTE abundance analysis. The effects of the non-local thermodynamic equilibrium for these two lines cannot be disregarded because the photoionization causes the ground state of the $4s^2S$ level to become depopulated, as we can see from Fig 5.1. Thus, the non-local thermodynamic equilibrium effects for these two lines cannot be neglected.

5.2 Analysis and results

In the analysis computed by Shi et al. (2014), twelve lines between 3100 Å $< \lambda <$ 8100 Å were used to infer the solar copper abundance. In Fig. 5.2 the best NLTE fits (continuous curves) of the solar lines (filled circles) are shown. The dashed curves show the synthetic spectra computed without copper in the atmosphere. We performed our analysis on the five lines at wavelength 5105.541, 5218.204, 5220.070, 5782.132, and 8092.634 Å, avoiding the remaining lines since they are too blended, and for this reason, they are not suited for our purpose. In Table 5.1, I present the parameters needed to determine the copper abundance for the selected lines, including wavelengths, transitions, and lower excitation energies. To perform the spectral line synthesis I used Balder (4.3), adopting a 1D solar model atmosphere with $Teff = 5777\ K$, $\log(g) = 4.44$, and a constant microturbulence velocity $\xi_t = 0.9\ km\ s^{-1}$. Once I obtained the synthetic spectrum both in LTE and NLTE, I apply the broadening with a Gaussian profile which accounts for instrumental broadening as well as macroturbulence and rotational broadening. To be precise, the rotational broadening has another functional form, which is not Gaussian, but studying the Sun, it is such a small contribution compared to the other components, that can be included in the Gaussian function. In particular, I convolved the spectra with different macroturbulence velocities (v) depending on the line. Finally, for each line, the best-fit value was investigated by varying the values of abundance and v, within a defined range, and by performing a χ^2 minimization. The minimization procedure calculates the squared residuals between the observed spectrum and the models, by varying the free parameters. The χ^2 is defined as a sum over all the pixels:

$$\chi^2(x) = \sum_{pixel} \frac{(x_{synthetic} - x_{atlas})^2}{\sigma} \tag{5.1}$$

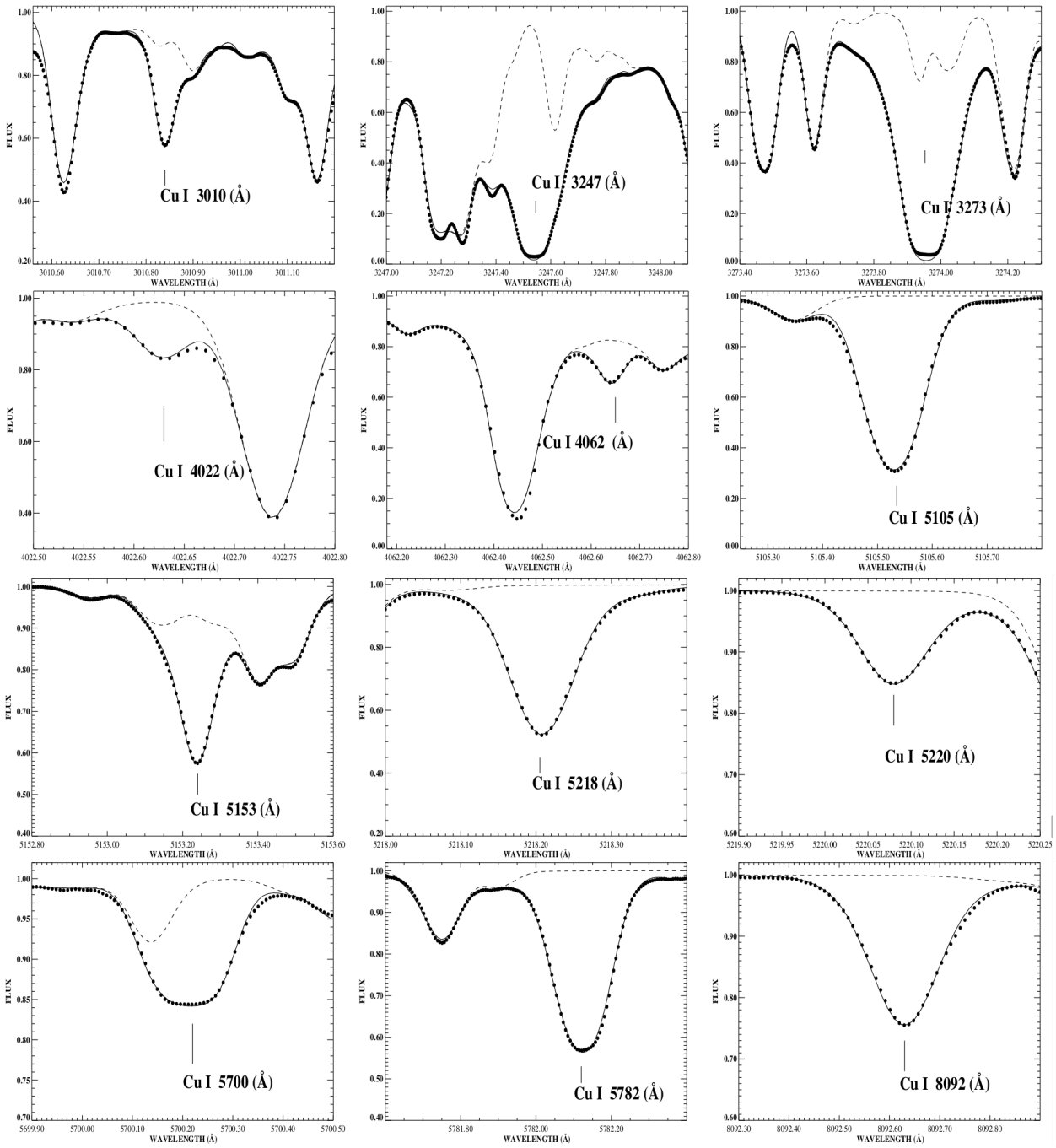

Figure 5.2: Lines analysed by Shi et al. (2014). Best NLTE fits (continuous curves) of the solar lines of Cu I (filled circles). Dashed curves show the synthetic spectra computed without copper in the atmosphere.

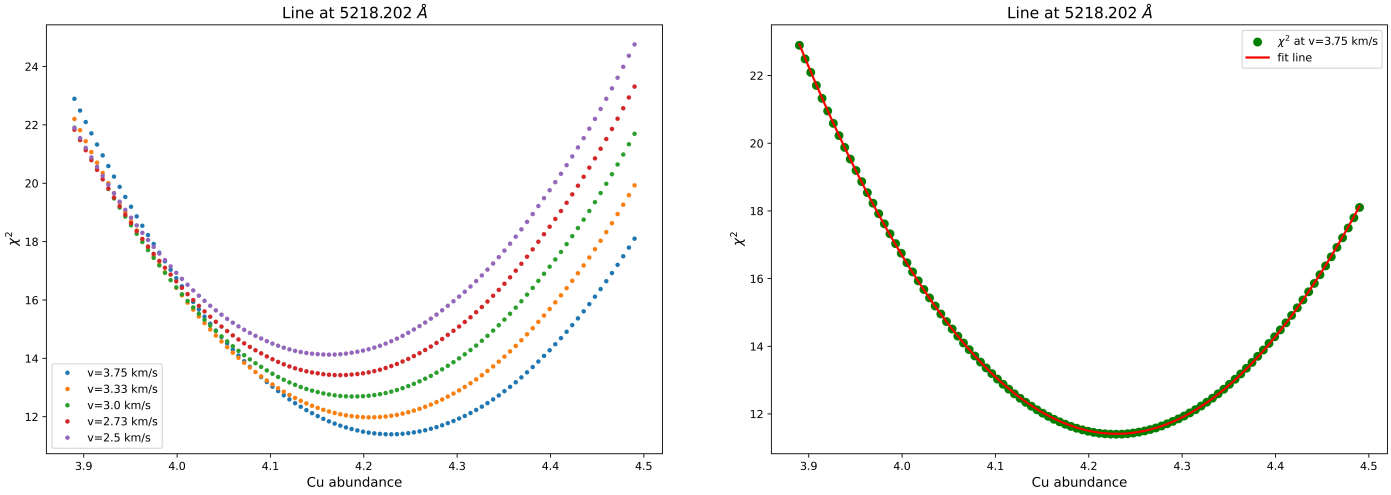

Figure 5.3: Left figure: χ-square distribution as a function of the Cu abundance, which is the free parameter, for five different values of resolution velocity. Right figure: this plot shows the parabolic fit of the curve which contains the minimum χ-square.

where $x_{synthetic}$ is the synthetic spectrum at a given abundance and convolved with a given v, while x_{atlas} is a solar spectral atlas obtained with the Fourier Transform Spectrometer at the McMath/Pierce Solar Telescope situated on Kitt Peak, Arizona. Finally, σ is the standard deviation of the flux. Plotting the χ^2 as a function of the free parameter value, I have obtained the minimization plots that in figures 5.3 are shown for the line at 5218.202 Å. The figure on the left shows the plot of the χ^2 distribution for five different values of the macroturbulence velocity as a function of the Cu abundance. It is immediately clear that the better fit is given by the synthetic line convolved with $v = 3.75\ km/s$ (light blue line). Thus, the minimization procedure was applied to that chi-square curve. The minimum of the χ^2 distribution, represented in fig. 5.3 on the right, corresponds to the best-fit value of the abundance and a unitary variation of the chi-squared around its minimum defines the upper and lower standard errors in the best-fit value. Since all my χ^2 curves were symmetric around the minimum, the upper and the lower errors result to be the same.
The plots of the chi-squared for the other lines are presented in the Appendix(7), in fig. 7.1 for NLTE in fig. 7.2 for LTE.

In table 5.1, I reported the Cu abundance values obtained for each line both in NLTE and in LTE with their error. Those values were used to perform the best fit for each line, which are shown below, in figure 7.3. By looking at the plots of the

lines, we immediately notice that none of the fits reproduces the trend of the wings coherently, and this is probably the reason why the minimum values of the chi-square are so high. Wings tend to come from gas at deeper and hotter layers which have more fast-moving atoms. This means that the thermal and collisional broadenings are relevant and need to be considered. Fortunately, Balder intrinsically computes the Voigt profile, which includes both the Gaussian and the Lorentzian broadenings. Thus, the bad fits could be caused by the one-dimensional hydrodynamic model we are using. First of all, as I mentioned above, implementing a 1D model means that the microturbulence is taken as a constant. In this case, it was fixed to 0.9 km^{-1}, according to Lind et al. (2022). Moreover, I convolved the synthetic spectra with a Gaussian profile in order to include the macroturbulence broadening as previously mentioned, but to build a more precise model I should have separated the different broadening contributions. Moreover, as I mentioned in section 4.3.1, 1D models do not reproduce realistically the convective motion on the stellar surface, and this can cause a mismatch between the observed lines and the synthetic ones.
Moreover, my synthetic spectrum was built only for copper. This is the reason why it does not fit properly the wings of some lines. For example, the lines at 5220.070 and at 8092.634 Å are blended to the right, and the line at 5782.132 Å is blended to the left with other spectral lines generated by the presence of other elements.

The mean value for Cu abundance obtained in NLTE is $log_{\epsilon_\odot} A(Cu) = 4.29 \pm 0.10$, where the error was calculated as the standard deviation of the mean. This value is compatible within 1σ with the one obtained by Shi et al. (2014) when adopting the gf values from Liu et al. (2014): $log_{\epsilon_\odot} A(Cu) = 4.19 \pm 0.09$. Both the results are perfectly consistent with the meteoritic value 4.25±0.05 of Lodders et al. (2009). The mean value is also compatible with the one reported by Asplund et al. (2021), which is the most updated present-day solar photospheric abundance catalogue for 83 long-lived elements. They believe the solar Cu abundance $log_{\epsilon_\odot} A(Cu) = 4.18 \pm 0.05$ of Grevesse et al. (2011) is the most reliable, despite it is based on old and relatively

λ(Å)	Transition	$E_{low}(Ev)$	A(Cu) NLTE	A(Cu) NLTE (Shi+14)	A(Cu) LTE	A(Cu) LTE (Shi+14)
5105.541	$4s^2\ ^2D_{5/2} - 4p\ ^2P^o_{3/2}$	1.389	4.25 ± 0.15	4.12	4.11 ± 0.17	4.10
5218.202	$4p\ ^2P^o_{3/2} - 4d\ ^2D_{5/2}$	3.817	4.23 ± 0.10	4.26	4.09 ± 0.11	4.24
5220.070	$4p\ ^2P^o_{3/2} - 4d\ ^2D_{3/2}$	3.817	4.30 ± 0.06	4.24	4.15 ± 0.05	4.23
5782.132	$4s^2\ ^2D_{3/2} - 4p\ ^2P^o_{1/2}$	1.642	4.35 ± 0.06	4.14	4.26 ± 0.06	4.13
8092.634	$4p\ ^2P^o_{3/2} - 5s\ ^2S_{1/2}$	3.817	4.30 ± 0.08	4.26	4.23 ± 0.08	4.31

Table 5.1: Wavelenght, transitions and lower energies of the five lines analysed. Cu abundance obtained in NLTE and LTE for each line, compared to the values found by Shi et al. (2014)

uncertain experimental oscillator strengths Kock and Richter (1968). Indeed, they declare that the newer theoretical gf-values of Liu et al. (2014) imply an unacceptably large line-to-line abundance scatter. However, the Cu abundance value we obtained is consistent also with the one by Grevesse et al. (2011).
The mean value in LTE is $log_{\epsilon_\odot} A(Cu) = 4.17 \pm 0.11$, it is compatible with the value found by Kock and Richter (1968), which is $log_{\epsilon_\odot} A(Cu) = 4.16 \pm 0.08.$, and with the value found by Shi et al. (2014) equal to $log_{\epsilon_\odot} A(Cu) = 4.17 \pm 0.10$.

In figure 5.4 the final results about copper abundance are shown. In the upper panels the NLTE abundance for the five lines, the mean copper abundance with the error, and the literature values of $log_{\epsilon_\odot} A(Cu)$ are reported. The comparison with Shi et al. (2014) and with Asplund et al. (2021) are shown on the left and on the right, respectively. In the lower panels of 5.4 we present our resulting LTE copper abundance compared to Shi et al. (2014) on the left and to Kock and Richter (1968) on the right. The consistency between our results and the ones in the literature is reasonable, even if the errors are bigger than Kock and Richter (1968) and Asplund et al. (2021). It is maybe due to the low number of lines we analysed. Moreover, the order of the errors could be related to all the reasons mentioned above, regarding the broadening mechanisms and the 1D model. Indeed, recently it was found that the one-dimension models for abundance analysis show systematic errors compared with threedimensional results (Bonifacio et al. (2010)). The solar metal abundances analyzed in three dimensions show slightly different results (Asplund et al. (2009)). Moreover, some recent analyses indicate that the LTE-3D corrections of Cu I resonance lines for turnoff metal-poor stars are large, while they are small for giant stars. Thus, also the solar abundance may need to consider the three-dimensional corrections (Asplund (2005)).

Finally, the plots in fig. 5.5 show the difference between the mean copper abundance calculated in NLTE and LTE. As mentioned many times, UV overionization is the primary NLTE mechanism for Cu I. Our work confirms that this effect causes systematically lower total absorption in the Cu I lines and, consequently, higher positive abundance corrections. However, we found a higher difference between the mean abundance calculated in NLTE and the one in LTE which results equal to 0.12 dex, than the one given by Shi et al. (2014), which is lower than 0.02 dex. Probably this discrepancy is due to the different datasets we used for collisions with hydrogen. Shi et al. (2014) used the so-called Drawin formula (Drawin (1969)) described by Steenbock and Holweger (1984), while we used the cross-sections calculated by Belyaev et al. (2020). From comparisons with full quantum calculations for several elements (Li, O, Na, Mg, Ca and Ni atoms) (Belyaev et al. (1999), Belyaev et al. (2010), Belyaev et al. (2012), Belyaev et al. (2019), Voronov et al. (2022)), it was discovered that the conventional formula proposed by Drawin is unreliable and fails to explain the fundamental processes involved in inelastic collisions with hydrogen.

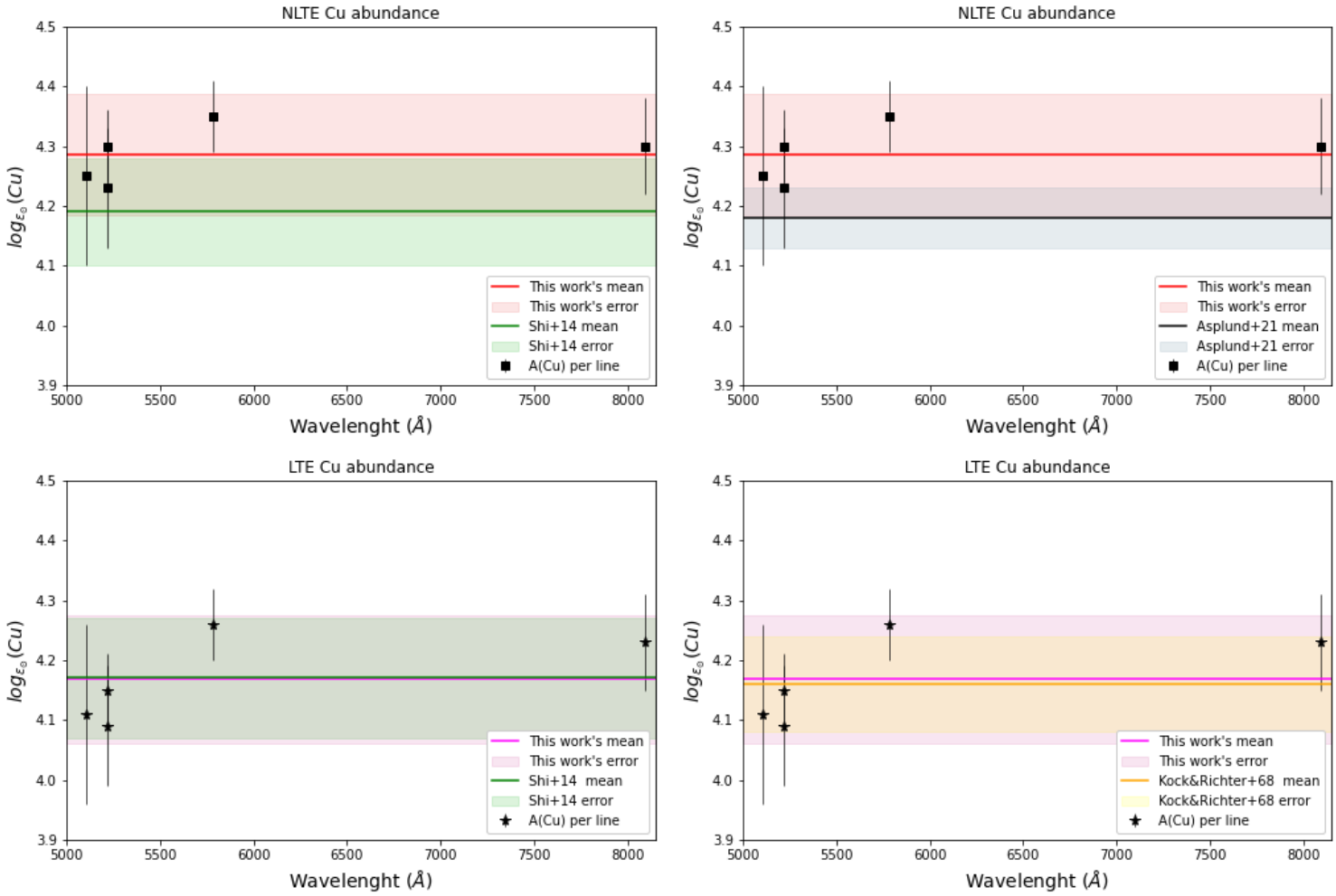

Figure 5.4: The four panels show the final result. The first, on the upper-left side, the squares represent the NLTE abundance for the five lines with their errors, the mean copper abundance with the error ($log_{\epsilon_\odot} A(Cu) = 4.29 \pm 0.10$), are given by the red line and the red faint areas, respectively. The green line gives the literature value by Shi et al. (2014). The second plot, on the upper-right side of $log_{\epsilon_\odot}$ shows the same result as before but compared to the Cu abundance mean value found by Asplund (2005), given by the black line. The plot on the lower panels shows our results for Cu abundance obtained in LTE, in magenta, and the literature results in green for Shi et al. (2014) and in yellow for Kock and Richter (1968).

In particular, Barklem et al. (2011) demonstrated that this formula provides data overestimated by several orders of magnitude for collisional processes associated with optically allowed transitions in atoms (copper in this case) and underestimates

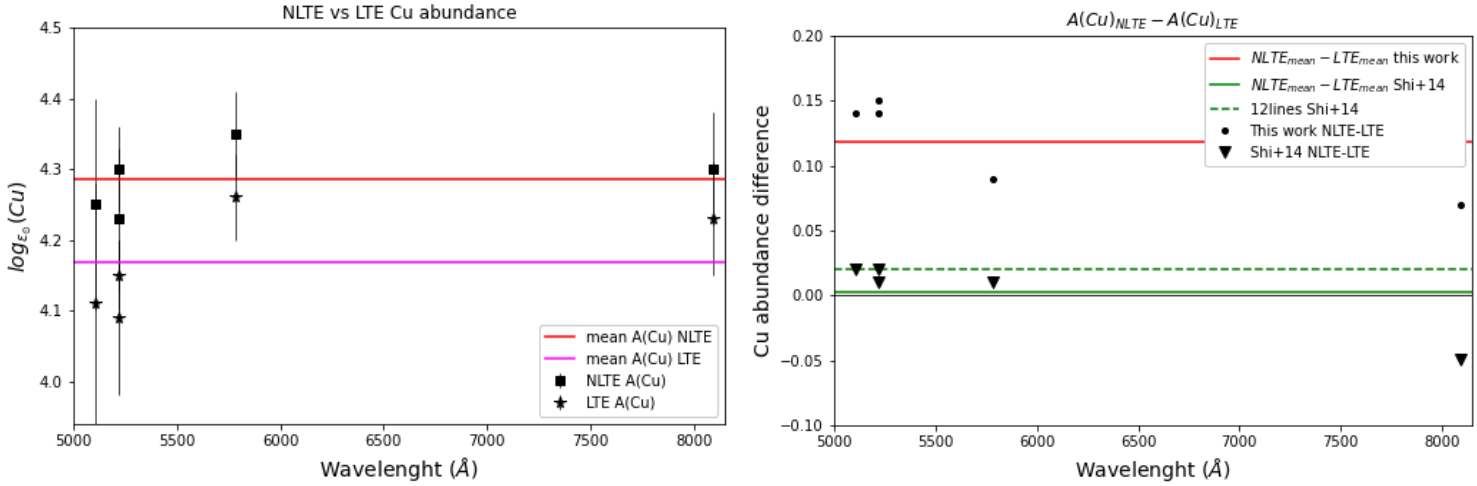

Figure 5.5: The panel on the left shows the Cu abundance for each line calculated both in NLTE (squares) and LTE (stars). The two red and magenta lines represent the mean abundances in NLTE and LTE respectively. In the plot on the right the difference between the abundance calculated in NLTE and LTE by this work and Shi et al. (2014) is presented. The circles and the triangles represent the difference for each line, obtained by us and by Shi et al. (2014) respectively. The red and green solid lines are the mean values obtained for the five lines in question. The green dashed line represents the $log_{\epsilon_\odot} A(Cu)_{NLTE} - log_{\epsilon_\odot} A(Cu)_{LTE}$ for 12 lines including the five we analysed.

the rates by several orders of magnitude for the processes associated with optically forbidden transitions. The approach used by Shi et al. (2014) to correct for inadequacies in the Drawin recipe is to scale the rate coefficients by an empirical factor S_H. This correction factor is commonly used since complete quantum calculations are time-consuming, especially for quantum-chemical data. However, recently, Belyaev et al. (2020) investigated the inelastic processes in low-energy $Cu + H \leftrightarrow Cu^+ + H^-$ collisions (306 partial processes in total) considering the fine-structure effects. And it provides us with an opportunity to explore the influence of the NLTE effects on copper lines when using accurate data.

Chapter 6

Conclusion

Astronomical spectroscopy is a branch of observational astrophysics that is becoming increasingly important nowadays. One of its main purposes is the study of stars. Through stellar spectroscopy, we can determine many of their properties, including their chemical composition. As we have already mentioned many times, the amount of chemical elements contained in the photosphere of stars reflects the amount present in the star-forming clouds from which they were born. Modern star-forming clouds have been enriched in chemical elements by generations of previous stars that, by exploding in Supernovae, have expelled their outermost layers. Heavier elements than iron, not contained in stars, are formed in neutron-capture processes during the explosions themselves or during collisions between neutron stars. Studying the chemical abundances in the photospheres of stars thus helps us understand how, where, when, and how often these kinds of events occur. Furthermore, it allows us to reconstruct the chronological history of these elements: how and when they were created in the Universe.

During my thesis work, I built a new model atom for copper based on the latest atomic data. The energy levels and bound-bound transition data were taken from the spectroscopic line calculation performed by Kurucz (1999). The hydrogen collisions data recently published by Belyaev et al. (2020). The accurate oscillator strengths for all the line transitions in model atom and photoionization cross sections were calculated by Liu et al. (2014), using the R-matrix method in the Russell–Saunders coupling scheme. The electron collisions rate were computed with a semi-empirical recipe. The radiative transfer calculations were performed in LTE and NLTE with a one-dimensional hydrodynamic model atmosphere, by the radiative transfer code Balder (Amarsi et al. (2019)).

As a result, I obtained a synthetic spectrum for copper in the Solar atmosphere, which I used to infer the NLTE and LTE copper abundance in the Sun, through the synthesis method. The final abundances in NLTE and LTE are $log_{\epsilon_\odot} A(Cu) = 4.29 \pm 0.10$ and $log_{\epsilon_\odot} A(Cu) = 4.17 \pm 0.11$ respectively. They were calculated as

the mean value of the abundances values inferred for five lines of Cu I, chosen by a set of twelve lines analyzed by Shi et al. (2014). The abundance of each line was found through a chi-squared minimization process and corresponds to the best-fit value. The results show that NLTE corrections are needed for Cu I Solar-type stars. The difference of 0.12 dex in the Cu abundance calculated in NLTE and LTE, indeed, is due to an NLTE mechanism called over-ionization. It is an important depopulation process for low-lying levels of atoms in their minority ionization stage in the atmospheric layers optically thin to ionizing radiation. For this reason, the abundance calculated in LTE is lower than the one calculated in NLTE. However, the difference value is much larger than the one obtained by Shi et al. (2014) which is lower than 0.02 dex. This is probably due to the different hydrogen collision data. Indeed we used the dataset released by Belyaev et al. (2018), while Shi et al. (2014) used the Drawin formula (Drawin (1969)), which was discovered to be unreliable since it does not reproduce correctly the inelastic collisional processes with hydrogen. In order to further check this assumption, we could, in the near future, infer the copper abundance for the six metal-poor stars studied by Korotin et al. (2018). In their paper, they concluded that the difference $log_{\epsilon_\odot} A(Cu)_{NLTE} - log_{\epsilon_\odot} A(Cu)_{LTE}$ becomes more relevant at lower metallicities, while it is approximately zero around solar metallicities, but they also used the Drawin formula.
Moreover, all the works previously cited as well as this one, are performed with a one-dimensional hydrodynamic model for the solar photosphere and, in general, there are no 3D-NLTE studies about copper in the literature. For this reason, one of the next steps will be to upgrade the model to a 3D one. With this procedure, we hope also to obtain better lines' fits.

Chapter 7

Appendix

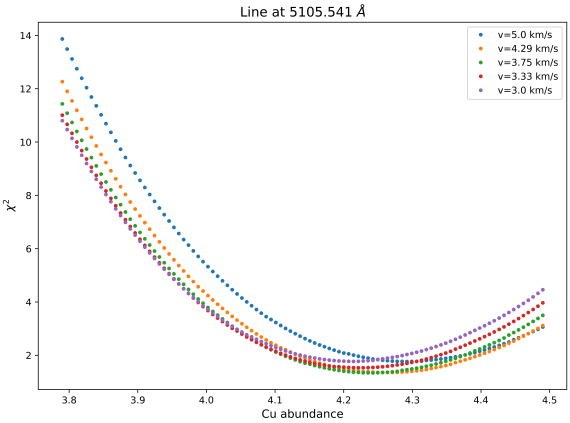
Line at 5105.541 Å
v=5.0 km/s
v=4.29 km/s
v=3.75 km/s
v=3.33 km/s
v=3.0 km/s
χ^2
Cu abundance

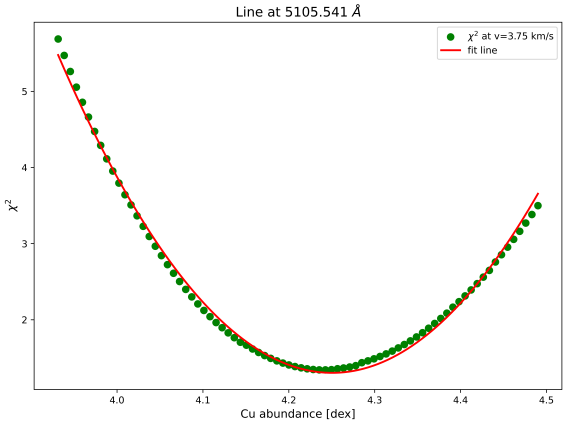
Line at 5105.541 Å
χ^2 at v=3.75 km/s
fit line
χ^2
Cu abundance [dex]

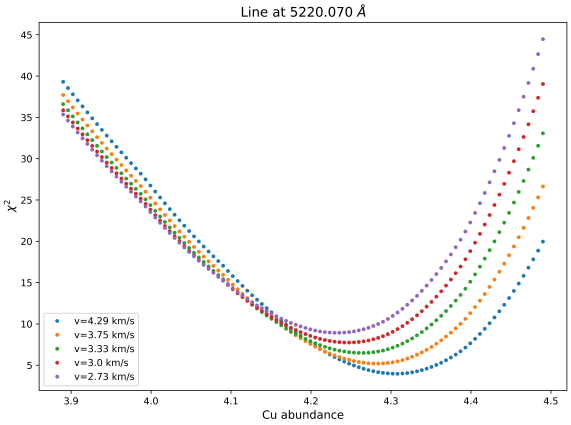
Line at 5220.070 Å
v=4.29 km/s
v=3.75 km/s
v=3.33 km/s
v=3.0 km/s
v=2.73 km/s
χ^2
Cu abundance

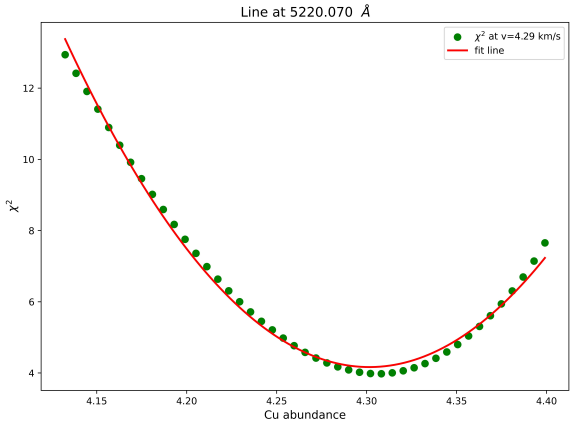
Line at 5220.070 Å
χ^2 at v=4.29 km/s
fit line
χ^2
Cu abundance

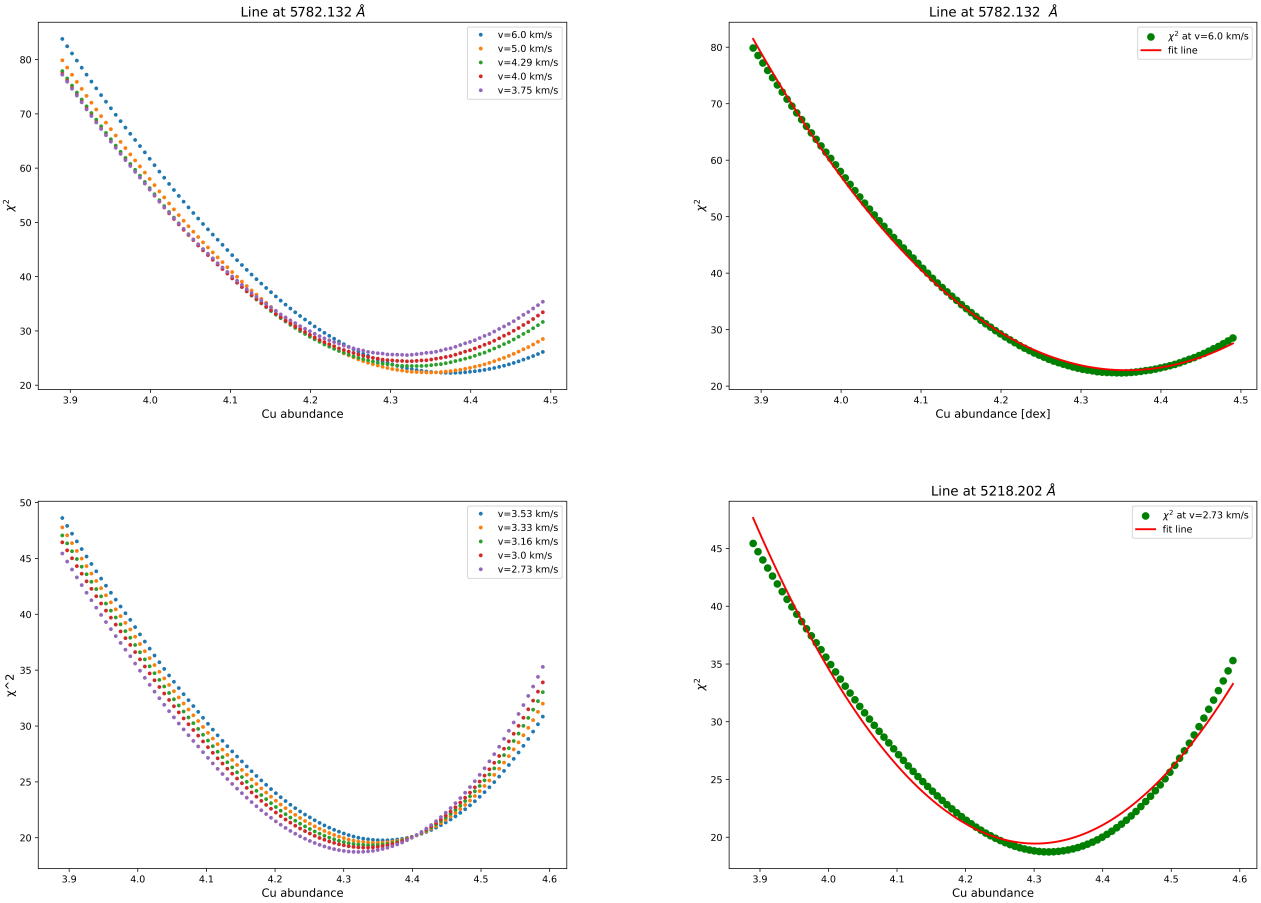

Figure 7.1: NLTE chi-square minimization procedure. Left figure: Chi-square distribution for different velocities. Right figure: parabolic fit that results in the best-fit abundance value.

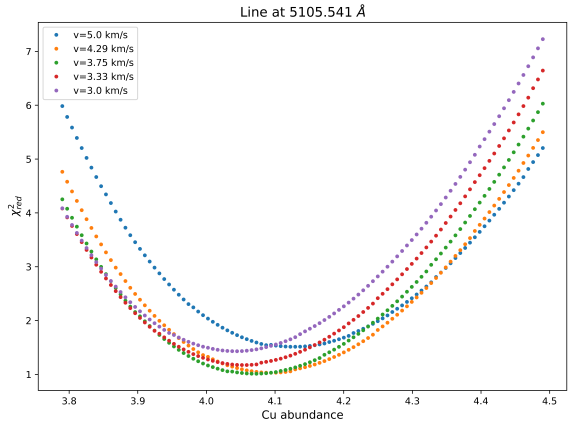
Line at 5105.541 Å
v=5.0 km/s
v=4.29 km/s
v=3.75 km/s
v=3.33 km/s
v=3.0 km/s
χ^2_{red}
Cu abundance

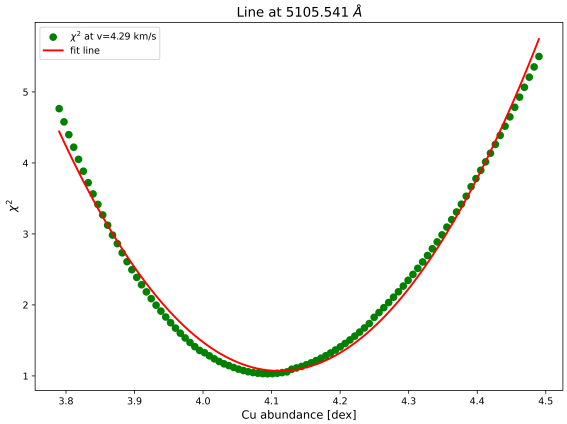
Line at 5105.541 Å
χ^2 at v=4.29 km/s
fit line
χ^2
Cu abundance [dex]

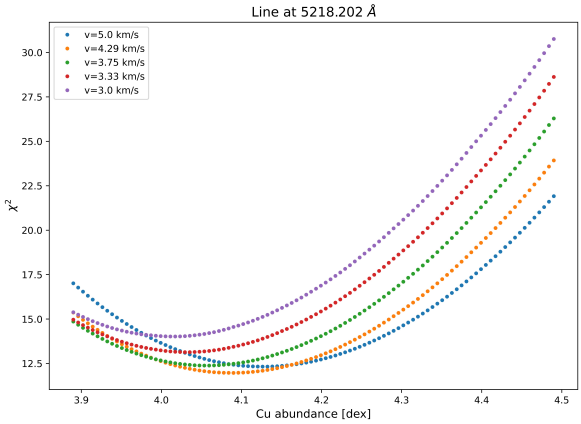
Line at 5218.202 Å
v=5.0 km/s
v=4.29 km/s
v=3.75 km/s
v=3.33 km/s
v=3.0 km/s
χ^2
Cu abundance [dex]

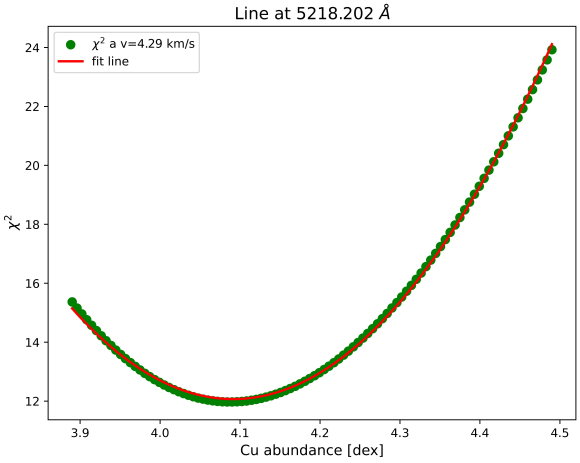
Line at 5218.202 Å
χ^2 a v=4.29 km/s
fit line
χ^2
Cu abundance [dex]

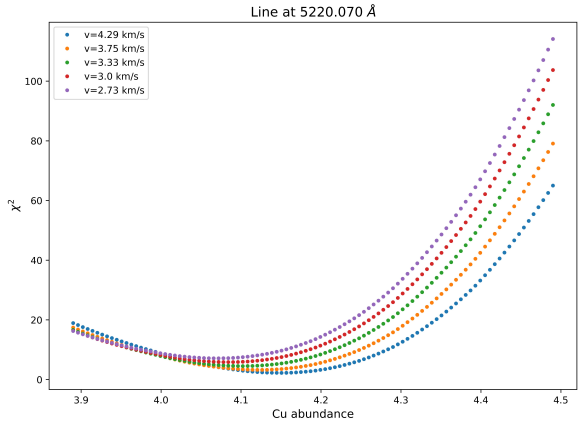
Line at 5220.070 Å
v=4.29 km/s
v=3.75 km/s
v=3.33 km/s
v=3.0 km/s
v=2.73 km/s
χ^2
Cu abundance

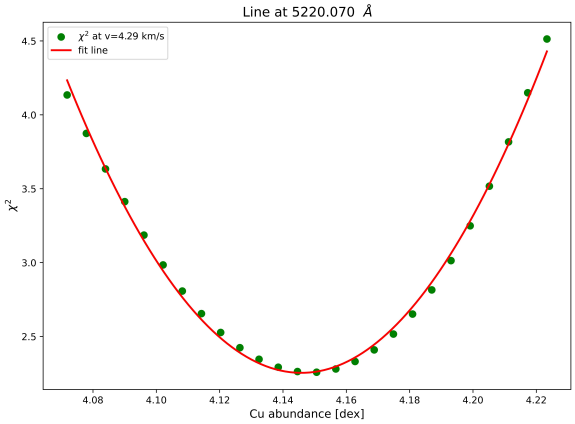
Line at 5220.070 Å
χ^2 at v=4.29 km/s
fit line
χ^2
Cu abundance [dex]

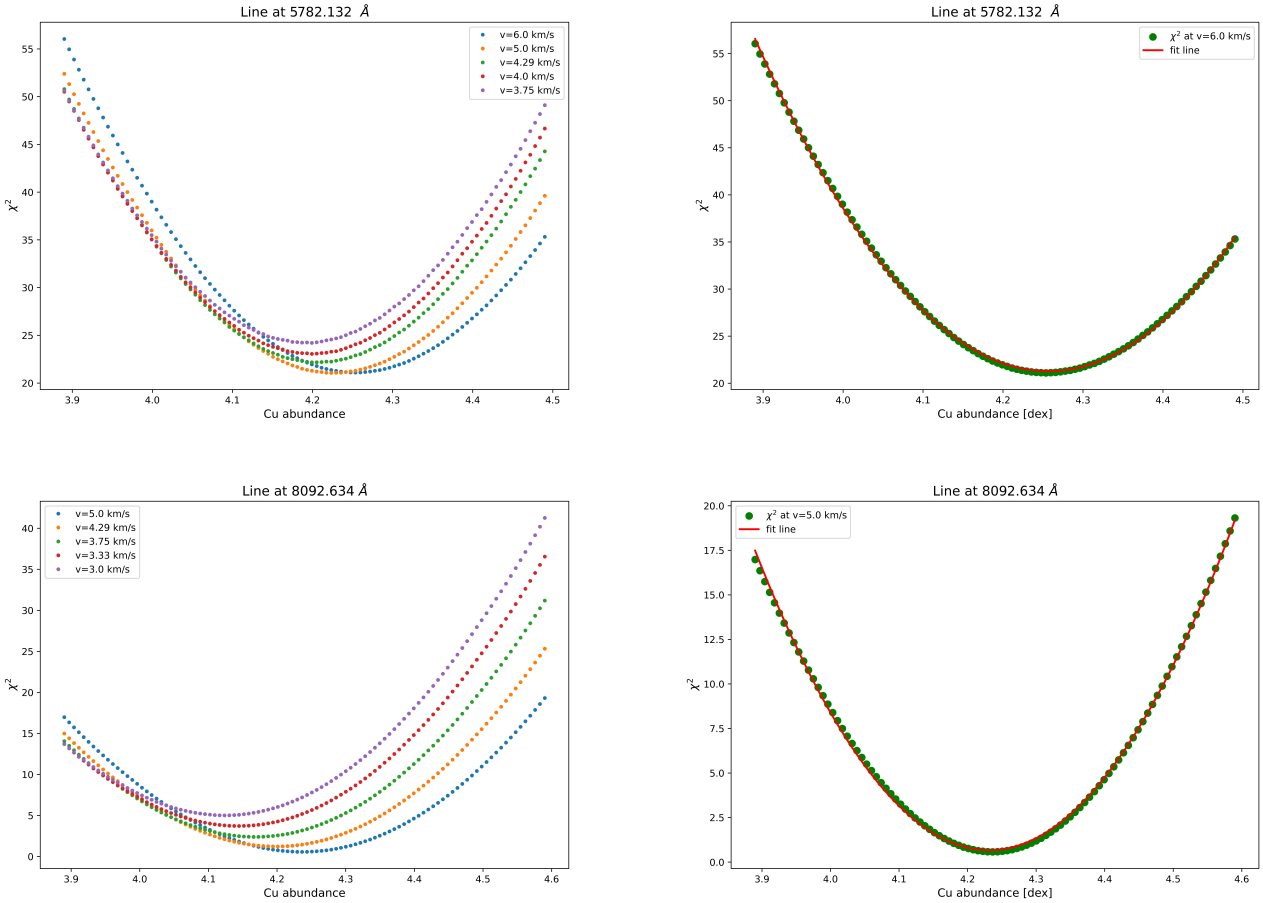

Figure 7.2: LTE chi-square minimization procedure. Left figure: Chi-square distribution for different velocities. Right figure: parabolic fit that results in the best fit abundance value.

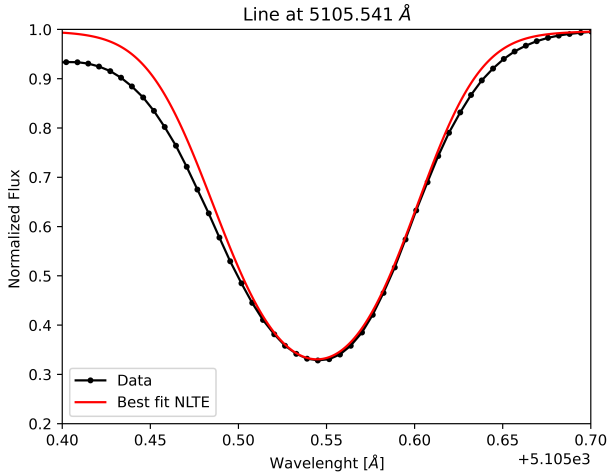
Line at 5105.541 Å
Normalized Flux
Wavelenght [Å]
+5.105e3
Data
Best fit NLTE

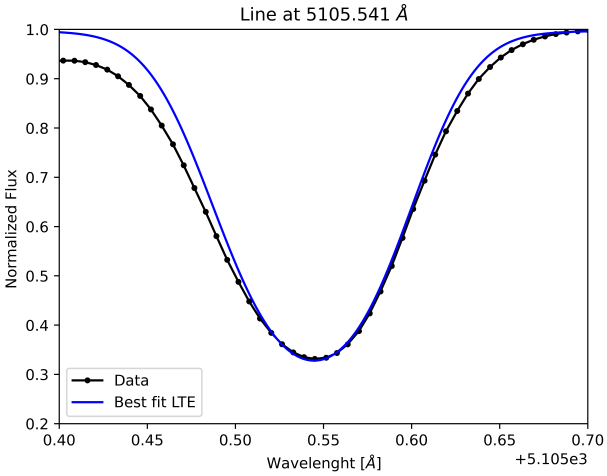
Line at 5105.541 Å
Normalized Flux
Wavelenght [Å]
+5.105e3
Data
Best fit LTE

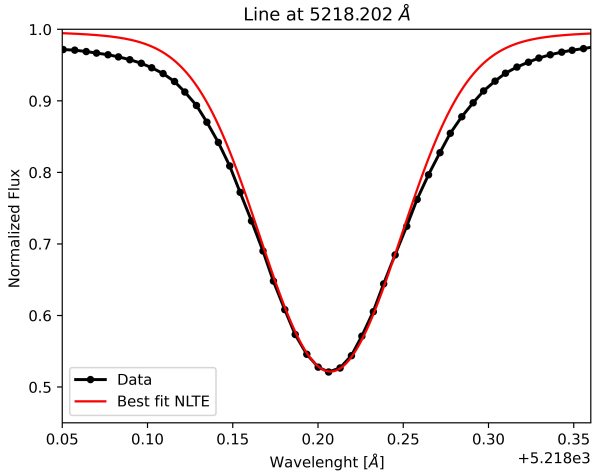
Line at 5218.202 Å
Normalized Flux
Wavelenght [Å]
+5.218e3
Data
Best fit NLTE

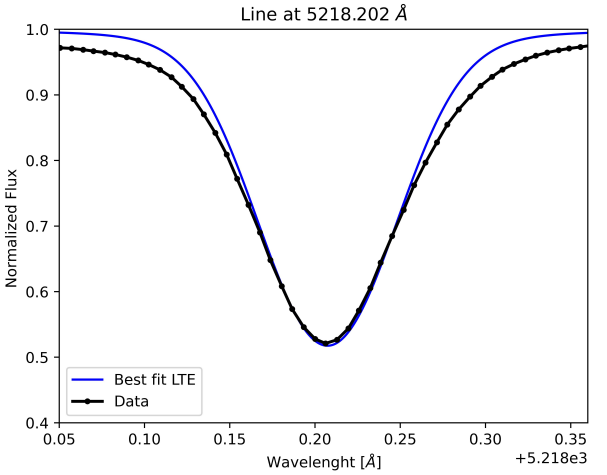
Line at 5218.202 Å
Normalized Flux
Wavelenght [Å]
+5.218e3
Best fit LTE
Data

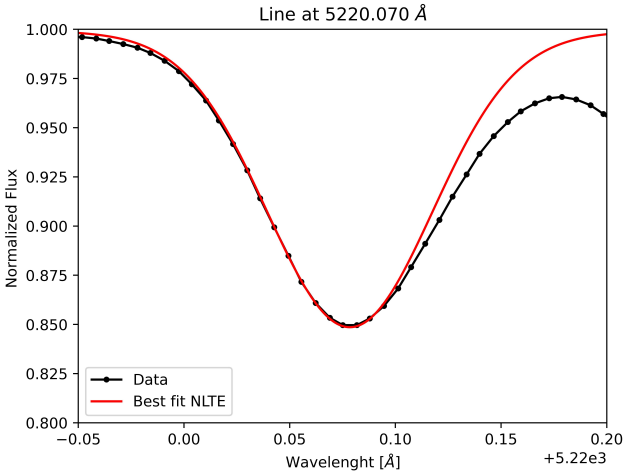
Line at 5220.070 Å
Normalized Flux
Wavelenght [Å]
+5.22e3
Data
Best fit NLTE

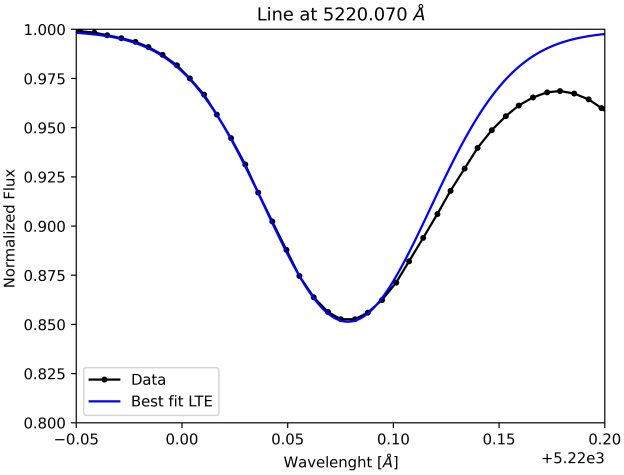
Line at 5220.070 Å
Normalized Flux
Wavelenght [Å]
+5.22e3
Data
Best fit LTE

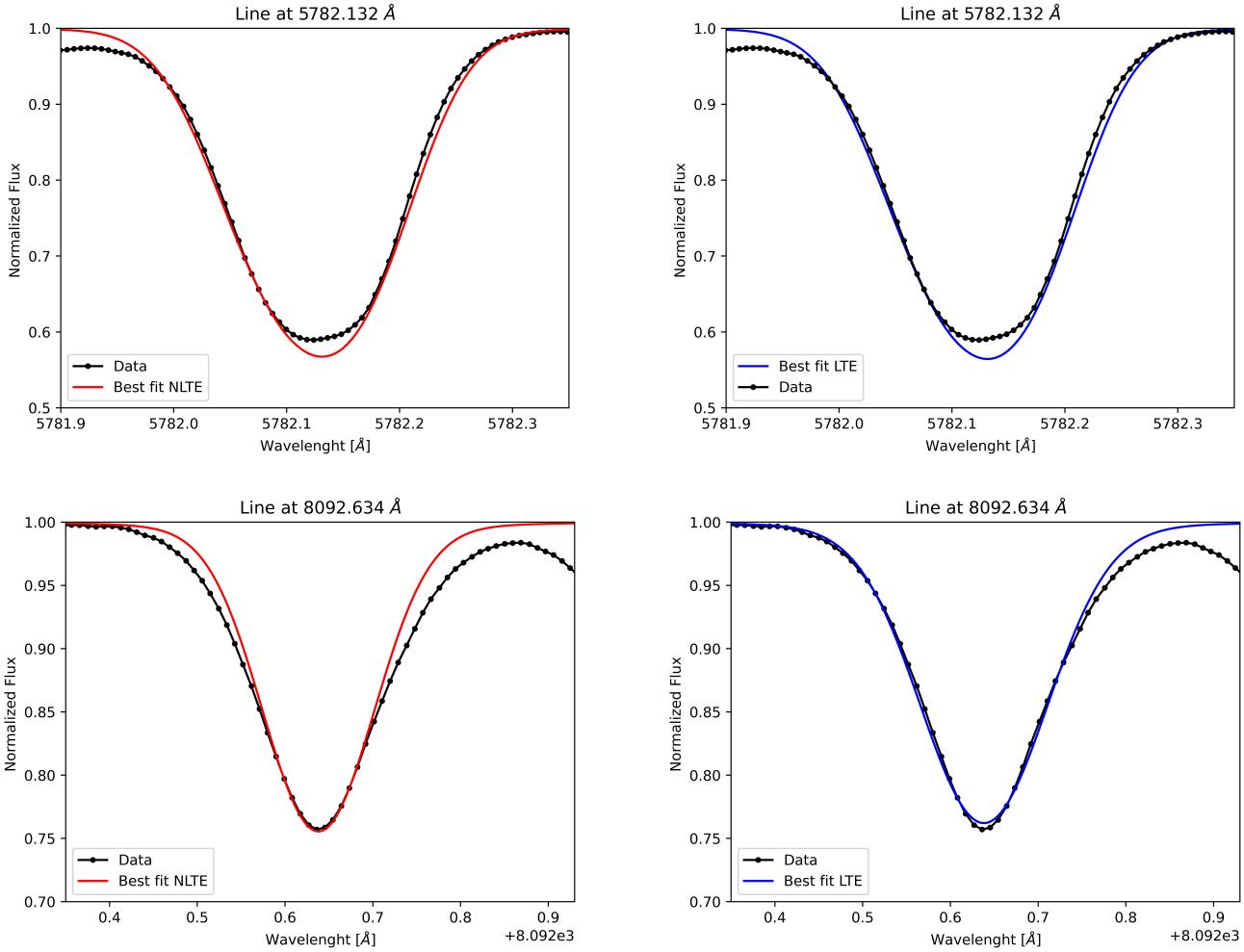

Figure 7.3: Left figure: NLTE best fit for each line. Right figure: LTE best fit for each line

Bibliography

Amarsi, A. M., Nissen, P. E., Asplund, M., Lind, K., and Barklem, P. S. (2019). Carbon and oxygen in metal-poor halo stars. *Astronomy & Astrophysics*, 622:L4.

Asplund, M. (2005). New light on stellar abundance analyses: Departures from lte and homogeneity. *Annual Review of Astronomy and Astrophysics*, 43:481–530. Copyright - Copyright Annual Reviews, Inc. 2005; Caratteristica del documento - Tables; Graphs; ; Ultimo aggiornamento - 2014-05-19.

Asplund, M., Amarsi, A. M., and Grevesse, N. (2021). The chemical make-up of the sun: A 2020 vision. *Astronomy and Astrophysics*, 653:A141.

Asplund, M., Grevesse, N., Sauval, A. J., and Scott, P. (2009). The chemical composition of the sun. *Annual Review of Astronomy and Astrophysics*, 47(1):481–522.

Barklem, P. S., Belyaev, A. K., Guitou, M., Feautrier, N., Gadéa, F. X., and Spielfiedel, A. (2011). On inelastic hydrogen atom collisions in stellar atmospheres. *Astronomy & Astrophysics*, 530:A94.

Bastian, N. and Lardo, C. (2018). Multiple stellar populations in globular clusters. *Annual Review of Astronomy and Astrophysics*, 56(1):83–136.

Baumgardt, H. and Hilker, M. (2018). A catalogue of masses, structural parameters, and velocity dispersion profiles of 112 milky way globular clusters. *Monthly Notices of the Royal Astronomical Society*, 478(2):1520–1557.

Belyaev, A. K., Barklem, P. S., Dickinson, A. S., and Gadéa, F. X. (2010). Cross sections for low-energy inelastic h^-. *Physical Review A*, 81(3):032706.

Belyaev, A. K., Barklem, P. S., Spielfiedel, A., Guitou, M., Feautrier, N., Rodionov, D. S., and Vlasov, D. V. (2012). Cross sections for low-energy inelastic mg + h and mg. *Physical Review A*, 85(3):032704.

Belyaev, A. K., Grosser, J., Hahne, J., and Menzel, T. (1999). Ab initio cross sections for low-energy inelastic h+na collisions. *Physical Review A*, 60(3):2151–2158.

Belyaev, A. K., Voronov, Y. V., and Gadéa, F. X. (2018). Data on inelastic processes in low-energy calcium hydrogen ionic collisions. *The Astrophysical Journal*, 867(2):87.

Belyaev, A. K., Voronov, Y. V., Mitrushchenkov, A., Guitou, M., and Feautrier, N. (2019). Inelastic processes in oxygen hydrogen collisions. *Monthly Notices of the Royal Astronomical Society*, 487(4):5097–5105.

Belyaev, A. K., Yakovleva, S. A., and Kraemer, W. P. (2020). Inelastic processes in copper–hydrogen collisions including fine-structure effects. *Monthly Notices of the Royal Astronomical Society*, 501(4):4968–4973.

Bergemann, M. and Nordlander, T. (2014). Non-lte radiative transfer in cool stars. theory and applications to the abundance analysis for 24 chemical elements. *ArXiv*.

Bihain, G., Israelian, G., Rebolo, R., Bonifacio, P., and Molaro, P. (2004). Cu and zn in the early galaxy. *Astronomy & Astrophysics*, 423(3):777–786.

Bisterzo, S., Gallino, R., Straniero, O., Cristallo, S., and Käppeler, F. (2010). s-Process in low-metallicity stars – I. Theoretical predictions. *Monthly Notices of the Royal Astronomical Society*, 404(3):1529–1544.

Böhm-Vitense, E. (1958). Über die wasserstoffkonvektionszone in sternen verschiedener effektivtemperaturen und leuchtkräfte. mit 5 textabbildungen. *Zeitschrift für Astrophysik*, 46:108.

Bonifacio, P., Caffau, E., and Ludwig, H.-G. (2010). Cu i resonance lines in turn-off stars of NGC 6752 and NGC 6397. *Astronomy & Astrophysics*, 524:A96.

Botnen, A. and Carlsson, M. (1999). Multi3d, 3d non-lte radiative transfer. In *Numerical Astrophysics*, pages 379–382. Springer Netherlands.

Cohen, J. G., Christlieb, N., McWilliam, A., Shectman, S., Thompson, I., Melendez, J., Wisotzki, L., and Reimers, D. (2008). New extremely metal-poor stars in the galactic halo. *The Astrophysical Journal*, 672(1):320–341.

Cox, A. N. (2000). *Allen's astrophysical quantities*. New York: AIP Press; Springer, 2000.

Drawin, H. W. (1969). Influence of atom-atom collisions on the collisional-radiative ionization and recombination coefficients of hydrogen plasmas. *Zeitschrift für Physik A Hadrons and nuclei*, 225(5):483–493.

Fuhrmann, K. (2008). Nearby stars of the Galactic disc and halo – IV. *Monthly Notices of the Royal Astronomical Society*, 384(1):173–224.

Grevesse, N., Asplund, M., Sauval, A., and Scott, P. (2011). The chemical composition of the sun. *Canadian Journal of Physics*, 89(4):327–331.

Ibgui, L., Hubeny, I., Lanz, T., and Stehlé, C. (2013). IRIS: a generic three-dimensional radiative transfer code. *Astronomy & Astrophysics*, 549:A126.

Iwamoto, K., Brachwitz, F., Nomoto, K. C. H. I., Kishimoto, N., Umeda, H., Hix, W. R., and Thielemann, F.-K. (1999). Nucleosynthesis in chandrasekhar mass models for type ia supernovae and constraints on progenitor systems and burning-front propagation. *The Astrophysical Journal Supplement Series*, 125(2):439–462.

Kock, M. and Richter, J. (1968). Experimentelle übergangswahrscheinlichkeiten und die solare häufigkeit des kupfers. *Zeitschrift für Astrophysik*, 69:180.

Korotin, S. A., Andrievsky, S. M., and Zhukova, A. V. (2018). Copper abundance from CuI and CuII lines in metal poor star spectra: NLTE versus LTE. *Monthly Notices of the Royal Astronomical Society*, 480(1):965–971.

Kurucz, R. L. (1999). Robert l. kurucz on-line database of observed and predicted atomic transitions.

Lind, K., Amarsi, A. M., Asplund, M., Barklem, P. S., Bautista, M., Bergemann, M., Collet, R., Kiselman, D., Leenaarts, J., and Pereira, T. M. D. (2017). Non-LTE line formation of Fe in late-type stars – IV. Modelling of the solar centre-to-limb variation in 3D. *Monthly Notices of the Royal Astronomical Society*, 468(4):4311–4322.

Lind, K., Nordlander, T., Wehrhahn, A., Montelius, M., Osorio, Y., Barklem, P. S., Afşar, M., Sneden, C., and Kobayashi, C. (2022). Non-lte abundance corrections for late-type stars from 2000 Å to 3 μm. i. na, mg, and al. *Astronomy and Astrophysics*, 665:A33.

Liu, Y. P., Gao, C., Zeng, J. L., Yuan, J. M., and Shi, J. R. (2014). ATOMIC DATA OF cu i FOR THE INVESTIGATION OF ELEMENT ABUNDANCE. *The Astrophysical Journal Supplement Series*, 211(2):30.

Lodders, K., Palme, H., and Gail, H.-P. (2009). 4.4 abundances of the elements in the solar system. In *Solar System*, pages 712–770. Springer Berlin Heidelberg.

McWilliam, A. and Smecker-Hane, T. A. (2005). The unusual abundance of copper in the sagittarius dwarf spheroidal galaxy and implications for the origin of ω centauri. *The Astrophysical Journal*, 622(1):L29–L32.

Mishenina, T. V., Kovtyukh, V. V., Soubiran, C., Travaglio, C., and Busso, M. (2002). Abundances of cu and zn in metal-poor stars: Clues for galaxy evolution. *Astronomy & Astrophysics*, 396(1):189–201.

Nordlander, T., Amarsi, A. M., Lind, K., Asplund, M., Barklem, P. S., Casey, A. R., Collet, R., and Leenaarts, J. (2016). 3d NLTE analysis of the most iron-deficient star, SMSS0313-6708. *Astronomy & Astrophysics*, 597:A6.

Pérez, A. E. G., Prieto, C. A., Holtzman, J. A., Shetrone, M., Mészáros, S., Bizyaev, D., Carrera, R., Cunha, K., García-Hernández, D. A., Johnson, J. A., Majewski, S. R., Nidever, D. L., Schiavon, R. P., Shane, N., Smith, V. V., Sobeck, J., Troup, N., Zamora, O., Weinberg, D. H., Bovy, J., Eisenstein, D. J., Feuillet, D., Frinchaboy, P. M., Hayden, M. R., Hearty, F. R., Nguyen, D. C., O'Connell, R. W., Pinsonneault, M. H., Wilson, J. C., and Zasowski, G. (2016). ASPCAP: THE APOGEE STELLAR PARAMETER AND CHEMICAL ABUNDANCES PIPELINE. *The Astronomical Journal*, 151(6):144.

Pignatari, M., Gallino, R., Heil, M., Wiescher, M., Käppeler, F., Herwig, F., and Bisterzo, S. (2010). The weak s-process in massive stars and its dependence on the neutron capture cross sections. *The Astrophysical Journal*, 710(2):1557–1577.

Pompéia, L., Hill, V., and Spite, M. (2005). Abundances in a large sample of stars in the LMC disk II. cu, sc, and s-elements and some relationships between elements. *Proceedings of the International Astronomical Union*, 1(S228):519–524.

Prochaska, J. X., Naumov, S. O., Carney, B. W., McWilliam, A., and Wolfe, A. M. (2000). The galactic thick disk stellar abundances. *The Astronomical Journal*, 120(5):2513–2549.

Raiteri, C. M., Gallino, R., Busso, M., Neuberger, D., and Kaeppeler, F. (1993). The weak s-component and nucleosynthesis in massive stars. *The Astrophysical Journal*, 419:207.

Roederer, I. U., Preston, G. W., Thompson, I. B., Shectman, S. A., Sneden, C., Burley, G. S., and Kelson, D. D. (2014). A search for stars of very low metal abundance. vi. detailed abundances of 313 metal-poor stars*. *The Astronomical Journal*, 147(6):136.

Romano, D. and Matteucci, F. (2007). Contrasting copper evolution in centauri and the milky way. *Monthly Notices of the Royal Astronomical Society: Letters*, 378(1):59–63.

Rutten, R. J. et al. (1995). *Radiative transfer in stellar atmospheres*. Sterrekundig Instituut Utrecht.

Rybicki, G. B. and Hummer, D. G. (1991). An accelerated lambda iteration method for multilevel radiative transfer. *Astronomy and Astrophysics*, 245:171–181.

Shi, J. R., Gehren, T., Zeng, J. L., Mashonkina, L., and Zhao, G. (2014). STATISTICAL EQUILIBRIUM OF COPPER IN THE SOLAR ATMOSPHERE. *The Astrophysical Journal*, 782(2):80.

Sneden, C., Gratton, R. G., and Crocker, D. A. (1991). Trends in copper and zinc abundances for disk and halo stars. *Astronomy and Astrophysics*, 246:354.

Sobeck, J. S., Simmerer, J., Ivans, I. I., Sneden, C., Fulbright, J. P., and Kraft, R. P. (2005). Manganese abundances in cluster and field stars. *Proceedings of the International Astronomical Union*, 1(S228):379–384.

Steenbock, W. and Holweger, H. (1984). Statistical equilibrium of lithium in cool stars of different metallicity. *Astronomy and Astrophysics*, 130:319–323.

Ting, Y.-S., Conroy, C., Rix, H.-W., and Cargile, P. (2018). The payne: self-consistent ab initio fitting of stellar spectra. *ArXiv*.

Travaglio, C., Hillebrandt, W., Reinecke, M., and Thielemann, F.-K. (2004). Nucleosynthesis in multi-dimensional SN ia explosions. *Astronomy & Astrophysics*, 425(3):1029–1040.

Trypsteen, M. F. M. and Walker, R. (2017). Analysis of the spectra. In *Spectroscopy for Amateur Astronomers*, pages 76–84. Cambridge University Press.

Voronov, Y. V., Yakovleva, S. A., and Belyaev, A. K. (2022). Inelastic processes in nickelHydrogen Collisions. *The Astrophysical Journal*, 926(2):173.